Interaction modelling of the thermomechanical behaviour of spatially-oriented graphene platelets (GPLs) reinforced polymer matrix

Ahmed Elmasry, Wiyao Azoti, Mohab Elmarakbi, Ahmed Elmarakbi

Interaction Modelling of the Thermomechanical Behaviour of Spatially-Oriented Graphene Platelets (GPLs) Reinforced Polymer Matrix

Ahmed Elmasry[1]✉, Wiyao Azoti[2,3] , Mohab Elmarakbi[1], Ahmed Elmarakbi[1]

Abstract

Graphene has a diversity of properties, making it an attractive candidate as a reinforcement material. To fully exploit these properties; robust mathematical models should be designed and developed. However, considering interactions between embedded GPLs is a challenging task. These interactions have an important contribution to the behaviour of nanocomposite material, and most of the available numerical and analytical literature ignore them. The current work discloses an integrated and computationally inexpensive approach to help discover new realistic graphene platelets (GPLs) nanocomposite model using analytical Multi-site (MS) scheme. The superiority of MS modelling is achieved by the consideration of the effect of the interaction between GPLs inclusions and their neighbourhood. Analytical One-site (OS) scheme is also utilised to derive the macroscopic response of the composite with random microstructures. The modelling techniques employed to derive the overall response of the composite are based on a thermomechanical kinematics integral equation. In addition to the analytical investigation, numerical characterisation using finite element modelling (FEM) is also performed on a representative volume element (RVE) to confront the analytical micromechanics formulation. GPLs are selected for modelling the graphene for which different orientation are considered within a Polyamide-Nylon 6 (GPL/PA6) matrix. Our study provides a promising framework approach for a coherent design of this category of materials.

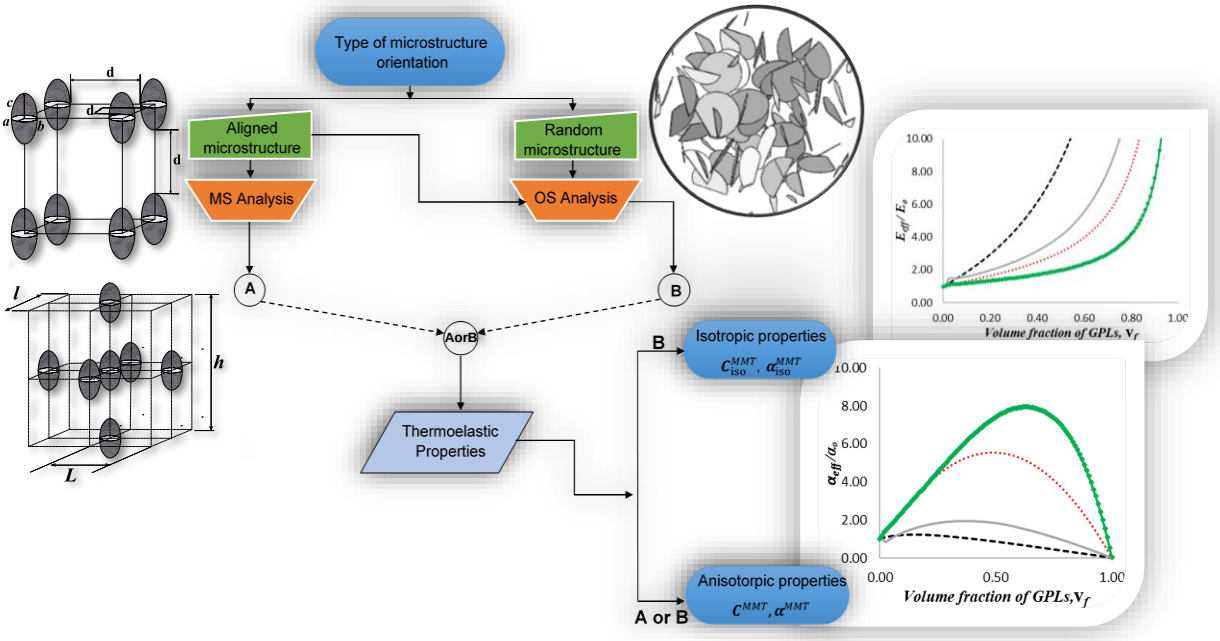

Keywords: Graphene platelets, Polymer matrix composites, Multi-site modelling, Thermoelastic properties, Micromechanics, RVE, FE modelling.

[1] Faculty of Engineering and Environment, Northumbria University, Newcastle upon Tyne, NE1.8ST, UK. [2] ICUBE Laboratory, CNRS UMR 7357, University of Strasbourg, 4 rue Boussingault, 67000 Strasbourg, France. [3] ECAM Strasbourg-Europe, School of Engineering, 2 rue de Madrid, 67300 Schiltigheim, France.

✉ Corresponding Author, E-mail: ahmed.elmasry@northumbria.ac.uk

1 Introduction

Multiphysics properties of the graphene make it an interesting candidate for composite reinforcements. To fully take advantage of these properties, the graphene must be uniformly well distributed in the matrix. As a critical parameter to enhance the mechanical properties of nanocomposite materials, the spatial orientation of the nano reinforcement (Ahmad et al., 2017; Gong, 2018) is of interest. The spatial orientation is defined by the topological texture of the microstructure. Indeed, the morphological and topological textures of the microstructure represent important design parameters in the effective response of the composite. These textures define the aspect ratio (AR), the orientation and the spatial distribution of the inclusion phases. In the case of so-called One-site (OS) modelling, only the interaction of the inclusion with the matrix is considered via the Eshelby tensor (Eshelby, 1957). This case remains the most discussed in the literature.

For the Multi-site (MS) modelling, the OS modelling is added to the interaction of the inclusion with its neighbourhood. This more complex modelling better accounts for the anisotropy of the composite through interaction tensors. Research works in that field were initiated by Fassi-Fehri and A. Hihi (1989) for the pairwise inclusions embedded within an anisotropic matrix. The MS modelling was used by Broohm et al. (2000) to predict the effective elastic properties of anisotropic material using an incremental micromechanics scheme. Numerical integration of the MS interactions tensors is derived in works by Zattarin (2000). The effective thermo-elastic properties of heterogeneous materials were predicted by Kpobie et al. (2012) using MS modelling. Recently, an extension of the MS scheme to the nonlinear composite materials was proposed by Azoti et al. (2015) for ordered microstructures.

In view of the spatial orientation of graphene in nanocomposites, various studies combining experimental techniques were conducted to refine their respective applications. Among these studies, one can distinguish experimental studies. Indeed, the anisotropic effect depending on the alignment direction has been investigated by Li et al. (2015a) on the photopermeability and thermal expansion of three types of graphene flakes: graphene oxide (GO), reduced GO and graphene platelets (GPLs) within an epoxy matrix composites. Using the polarised Raman spectroscopy, Li et al. (2015b) have quantified the spatial orientation of graphene by an orientation distribution function ODF. They concluded that their analysis could form a controllable relationship between the mechanical properties of nanocomposites and graphene orientation. Li et al. (2016) followed the same approach of Li et al. (2015b) using Raman

spectroscopy to study the spatial orientation of graphene oxide flakes in different nanocomposites and to estimate the orientation effect of the graphene reinforcement on Young's modulus. Boothroyd et al. (2018) investigated the controlling of graphene platelet (GPL) orientation and dispersion within a polymeric composite through continuous oscillatory shear and anneal processing. They showed that they have a huge impact on the composite conductivity and electrical properties. Besides, analytical methods have been used along with experiments to account for the spatial orientation of nanoparticles. Graphene. The Halpin– Tsai and Mori–Tanaka methods were implemented by Weon and Sue (2005) to account for the aspect ratio (AR) and the degree of orientation on nylon-6/clay nanocomposite. Comparative micromechanics works by Liu and Brinson (2008) have shown that nanoplatelets allow better mechanical reinforcing efficiency for most cases of random orientation compared to nanotubes. Based on a modified rule of mixtures for hybrid composite consisting of glass fibres (GF) and GPLs with polypropylene matrix, Papageorgiou et al. (2016) derive the effective Young's modulus. The orientation of the GF was obtained by SEM while polarised Raman spectroscopy was used for the orientation of the GPLs. Young et al. (2018) used a rule of mixtures accounting for the orientation of the reinforcing particles to predict the stiffness of the graphene nanocomposites consisted of nanoplatelets arranged between layers of a polymer matrix. Feng et al. (2017) investigated graphene platelets re-orientation under uni-axial stretching and bi-axial loading (Feng et al., 2018) on the Young's modulus of polymer nanocomposites. It is found that GPLs tend to re-align along stretching directions. Compared to uni-axial stretching, Young's modulus is increased along the stretching axes while decreased in the transverse direction, i.e. it depends on the stretching direction. They modelled the overall mechanical properties using the Mori-Tanaka homogenisation scheme for all possible orientations.

Besides, composite materials are often subjected to thermomechanical loads. The study of the thermomechanical properties allows a better understanding of their behaviour. It also gives a precise estimation of the reliability of composite materials under multi-physical loadings. Therefore, it is important to determine the thermomechanical properties of each phases within the composite. Investigations on graphene CTE reported unusual negative linear coefficient of thermal expansion (CTE) as reported by several authors (Fisher, 2018; Mann et al., 2017; Yoon et al., 2011). From molecular dynamics simulations (Shiu and Tsai, 2014; Shokrieh et al., 2014; Wang et al., 2018) to effective theoretical formulations (Sadowski et al., 2015; Su et al., 2018), as well as Finite element modelling (FEM) (Georgantzino et al., 2017; Xiao et al., 2018; Zhang et al., 2016), or combined experimental and numerical methods (Wejrzanowski et al., 2016;

Zarasvand and Golestanian, 2017), the thermal and mechanical properties of graphene-related composites were investigated versus the volume fraction, the size aspect ratio and the spatial orientation of the graphene. From computational and numerical modelling viewpoints, a number of 3D unit cell models with various nano reinforcements, different aspect ratios (ARs), shapes, orientations (aligned/ random) were generated using the program code for the automatic generation of finite element (FE) unit cells with multiple disk-shaped platelets and tested in numerical experiments (Dai and Jr., 2013, 2014; Jr. and Dai, 2014). However, the numerical simulations of multiscale composites have not reached their full potential yet, as the effects of several parameters (e.g. thermal, spatial orientation, etc.) still need to be considered for further investigations. The complications of mesh generation due to arbitrariness in the shape of inclusions represent a challenge, especially for small size inclusions where minuscule discretization levels are required—with significant limitations of high computational cost and time.

Although the MS approach has the advantage of dealing with the material's anisotropy through the morphological and topological textures of the microstructure, it appears from the above-mentioned works that accounting for an MS modelling of the interaction between the inclusions and their neighbourhood remains very less addressed.

The objective of this work is to propose a thermo-mechanical response of the effective behaviour of graphene in MS modelling. The transition scale is made by the global strain concentration tensor within the phases. It is obtained from the thermo-mechanical integral equation by Ahaouari et al. (1990), leading to an MS version of the Mori-Tanaka scheme (Kpobie et al., 2012). The anisotropy of the composite is accounted for through the interaction due to neighbourhood of inclusions. Herein, the neighbourhood used in works by Azoti et al. (2015) is adopted. Random as well as aligned configurations of orientations are analysed for the graphene reinforced composite. The analytical modelling is accompanied by FEM modelling for validation purposes. A 3D representative volume element (RVE) models subject to thermomechanical loading is then generated for microstructures and calculations of effective thermomechanical properties carried out under Abaqus.

The following organisation is adopted for the paper. Section2 establishes the analytical framework of a Multi-site micromechanics homogenisation for thermoelastic phases. This section presents the global strain concentration tensor and derives the effective properties

according to the Mori-Tanaka scheme for both random and ordered microstructures. Section3 deals with the 3D RVE FEM and the post-processing of the effective properties in Abaqus. The validation with respect to literature data on graphite Gt/Cu composite is done in Section 4. In this section, the OS and MS analytical results for both random and aligned inclusions are compared with FE calculations for the GPL/PA6 composite.

2 Analytical framework

2.1 Micromechanics and kinematics formulation

Considering an RVE of a micro- heterogeneous material that consists of $N+1$ reinforcements embedded in a continuous constituent regarded as a matrix (phase 0). At the microscopic scale, each constituent undergoes a total local strain $\boldsymbol{\varepsilon}(\boldsymbol{r})$. Admissible macroscopic static or kinematic loads are applied on the RVE boundaries in the absence of body forces and inertia terms. Decomposition of $\boldsymbol{\varepsilon}(\boldsymbol{r})$ into elastic $\boldsymbol{\varepsilon}^{e}(\boldsymbol{r})$ and thermal $\boldsymbol{\varepsilon}^{T}(\boldsymbol{r})$ parts can be considered as:

$$\boldsymbol{\varepsilon}(\boldsymbol{r}) = \boldsymbol{\varepsilon}^{e}(\boldsymbol{r}) + \boldsymbol{\varepsilon}^{T}(\boldsymbol{r}) \tag{1}$$

Using the Hooke law, the local stress $\boldsymbol{\sigma}(\boldsymbol{r})$ within the RVE yields:

$$\boldsymbol{\sigma}(\boldsymbol{r}) = \boldsymbol{c}(\boldsymbol{r}) : \boldsymbol{\varepsilon}(\boldsymbol{r}) - \boldsymbol{\beta}(\boldsymbol{r})\Delta T \tag{2}$$

where $\boldsymbol{\beta}(\boldsymbol{r}) = \boldsymbol{c}(\boldsymbol{r}) : \boldsymbol{\alpha}(\boldsymbol{r})$. In the above equations, $\boldsymbol{c}(\boldsymbol{r})$ and $\alpha(\boldsymbol{r})$denote the local elastic stiffness and thermal expansion tensor, respectively. The local thermal strain is written such as $\boldsymbol{\varepsilon}^{T}(\boldsymbol{r}) = \Delta T\boldsymbol{\alpha}(\boldsymbol{r})$ and ΔT representing an increment of the temperature, considering that for isotropic phases $\alpha_{ij}(\boldsymbol{r}) = \alpha^{r}\delta_{\mathrm{ij}}$ where $\alpha^{r}$is scalar thermal expansion coefficient and δ is Kronecker's delta. The operator **":"** stands for the tensorial contraction over two indices. The micromechanics scale transition consists, firstly, in the localization of the macroscopic strain tensor $\boldsymbol{E}$ through a fourth-order global strain concentration tensors $\boldsymbol{A}(\boldsymbol{r})$ and a second-order global strain concentration tensor $\boldsymbol{a}(\boldsymbol{r})$. Secondly, a homogenisation step uses averaging techniques $(\bullet)^{eff} = \overline{(\bullet)} = \frac{1}{V}\int_{V}(\bullet)dV$ to approximate the macroscopic behaviour. Note that $\boldsymbol{A}(\boldsymbol{r})$and $\boldsymbol{a}(\boldsymbol{r})$ remain unknown parameters that contain all the information about the

microstructure. The effective thermo-elastic properties of the RVE based on the average theorems due to (Hill, 1963), and (Mandel, 1971), are given by:

$$\boldsymbol{C}^{eff} = \frac{1}{V}\int_V \boldsymbol{c}\,(r)\colon \boldsymbol{A}(r)dV \tag{3}$$

$$\boldsymbol{\beta}^{eff} = \frac{1}{V}\int_V \boldsymbol{\beta}(\boldsymbol{r}) - \boldsymbol{c}(\boldsymbol{r})\colon \boldsymbol{a}(\boldsymbol{r})\,dV \tag{4}$$

where $\boldsymbol{C}^{eff}$ (or $\boldsymbol{S}^{eff} = \boldsymbol{C}^{eff^{-1}}$) and $\boldsymbol{\beta}^{eff}$ (or $\boldsymbol{\alpha}^{\text{eff}} = \boldsymbol{C}^{eff^{-1}}\colon \boldsymbol{\beta}^{eff}$) define equivalent thermo-elastic properties of the RVE. The global strain concentration tensor $\boldsymbol{A}(r)$ links the local strain $\boldsymbol{\varepsilon}(\boldsymbol{r})$ to the macroscopic strain $\boldsymbol{E}$ as follows:

$$\boldsymbol{\varepsilon}(\boldsymbol{r}) = \boldsymbol{A}(\boldsymbol{r})\colon \boldsymbol{E} + \Delta T\boldsymbol{a}(\boldsymbol{r}) \tag{5}$$

The decomposition of the local uniform thermo-elastic moduli into homogeneous reference parts $\boldsymbol{c}^R$ and $\boldsymbol{\beta}^R$, and fluctuation parts $\delta\boldsymbol{c}(\boldsymbol{r})$ and $\delta\boldsymbol{\beta}(\boldsymbol{r})$ such as:

$$\begin{aligned}\boldsymbol{c}(\boldsymbol{r}) &= \boldsymbol{c}^R - \delta\boldsymbol{c}(\boldsymbol{r})\\ \boldsymbol{\beta}(\boldsymbol{r}) &= \boldsymbol{\beta}^R - \delta\boldsymbol{\beta}(\boldsymbol{r})\end{aligned} \tag{6}$$

and their substitution within the equilibrium equation $\sigma_{ij,j}(\boldsymbol{r}) = 0$ along with Eq.(2) and the deformation's compatibility equation $\varepsilon_{ij}(\boldsymbol{r}) = \frac{1}{2}[u_{i,j}(\boldsymbol{r}) + u_{j,i}(\boldsymbol{r})]$ and a time derivative of the resulting equation leads to the integral kinematics equation established by Ahaouari (1990) and Ahaouari et al. (1990), for a thermo-elastic phase:

$$\boldsymbol{\varepsilon}(\boldsymbol{r}) = \boldsymbol{E}^R - \int_Y \boldsymbol{\Gamma}(\boldsymbol{r}-\boldsymbol{r}')\colon[\delta\boldsymbol{c}(\boldsymbol{r}')\colon\boldsymbol{\varepsilon}(\boldsymbol{r}') - \Delta T\delta\boldsymbol{\beta}(\boldsymbol{r}')]dV' \tag{7}$$

where $\boldsymbol{E}^R$ is the strain field inside the reference infinite medium subjected to the same boundary conditions as RVE and $\boldsymbol{\Gamma}(\boldsymbol{r}-\boldsymbol{r}')$ is the modified Green tensor, based on the fundamental Green solution of elasticity.

2.2 Global strain concentration tensors

The kinematic integral Eq.(7) represents the formal solution from which the global strain concentration tensor is derived from. Its substitution, into the average local strain of the Ith phase $\boldsymbol{\varepsilon}^I = \frac{1}{V}\int_V \boldsymbol{\varepsilon}(\boldsymbol{r})dV$ along with the fact $\boldsymbol{\varepsilon}^I$ can be written such that $\boldsymbol{\varepsilon}^I = \zeta^I : \boldsymbol{E}^R + \Delta T \mathfrak{z}^I$, leads to the global strain concentration tensors $\boldsymbol{A}^I$ and $\boldsymbol{a}^I$ for a Ith phase of the RVE such as (Kpobie et al., 2012):

$$\begin{cases} \boldsymbol{A}^I = \zeta^I : (\overline{\zeta}^I)^{-1} \\ \overline{\boldsymbol{A}}^I = \mathbf{I} \\ \boldsymbol{a}^I = \mathfrak{z}^I - \boldsymbol{A}^I : \overline{\mathfrak{z}}^I \\ \overline{\boldsymbol{a}}^I = 0 \end{cases} \tag{8}$$

where $\mathbf{I}$ is the fourth-order symmetric identity tensor and $\overline{(\bullet)}$ denotes the volume average of $(\bullet)$ over the considered RVE. The quantities $\boldsymbol{\zeta}^I$ and $\mathfrak{z}^I$ are the elastic and thermal strain local concentration tensors, respectively. with respect to the reference medium $\boldsymbol{E}^R$ and the temperature increment ΔT. These local concentration tensors $\boldsymbol{\zeta}^I$ and $\mathfrak{z}^I$ are given by (Kpobie et al., 2012):

$$
\begin{cases}
\zeta^{\boldsymbol{I}}_{(0)} = \left(\mathbf{I} + \boldsymbol{T}^{II} : (\boldsymbol{c}^{I} - \boldsymbol{c}^{R})\right)^{-1} \\
\mathfrak{Z}^{I}_{(0)} = \zeta^{I}_{(0)} : \boldsymbol{T}^{II} : \Delta\boldsymbol{\beta}^{I} \\
\zeta^{\boldsymbol{I}}_{(i+1)} = \left(\mathbf{I} + \boldsymbol{T}^{II} : (\boldsymbol{c}^{I} - \boldsymbol{c}^{R})\right)^{-1} : \left(\mathbf{I} - \sum_{\substack{J=0 \\ J \neq I}}^{N} \boldsymbol{T}^{IJ} : (\boldsymbol{c}^{J} - \boldsymbol{c}^{R}) : \zeta^{J}_{(i)}\right) \\
\mathfrak{Z}^{\boldsymbol{I}}_{(i+1)} = (\mathbf{I} + \boldsymbol{T}^{II} : (\boldsymbol{c}^{I} - \boldsymbol{c}^{R}))^{-1} : \left[\boldsymbol{T}^{II} : \Delta\boldsymbol{\beta}^{I} + \sum_{\substack{J=0 \\ J \neq I}}^{N} \boldsymbol{T}^{IJ} : \left(\Delta\boldsymbol{\beta}^{J} - (\boldsymbol{c}^{J} - \boldsymbol{c}^{R}) : \mathfrak{Z}^{J}_{(i)}\right)\right] \\
I = 0, 1, 2, \dots, N
\end{cases}
\tag{9}
$$

where subscripts (i) et $(i+1)$ are the iteration step numbers, whereas $\Delta\boldsymbol{\beta}^{I} = \boldsymbol{\beta}^{I} - \boldsymbol{\beta}^{R}$ and $\Delta\boldsymbol{\beta}^{J} = \boldsymbol{\beta}^{J} - \boldsymbol{\beta}^{R}$. N the number of phases considered in the composite (excluding the matrix phase (o)). To start this iterative process, initial approximation values of $\zeta^{\boldsymbol{I}}_{(0)}$and $\mathfrak{Z}^{I}_{(0)}$ leading to converging, are obtained by neglecting the influence of all constituents on relative concentration tensors of Ith element (Kröner, 1973, 1977). $\boldsymbol{T}^{II}$and $\boldsymbol{T}^{IJ}$ are the interaction tensors in One-site (OS) and Multi-site (MS) version, respectively. General expressions for $\boldsymbol{T}^{II}$ and $\boldsymbol{T}^{IJ}$ as well as their numerical implementation can be found in such as (Azoti et al., 2015):

$$
\begin{aligned}
\boldsymbol{T}^{IJ}(\boldsymbol{c}^{r}) &= \frac{1}{V^{I}} \int_{V^{I}} \int_{V^{J}} \boldsymbol{\Gamma}(\boldsymbol{r} - \boldsymbol{r}')\, dV' dV \\
\boldsymbol{T}^{II}(\boldsymbol{c}^{r}) &= \frac{1}{V^{I}} \int_{V^{I}} \int_{V^{I}} \boldsymbol{\Gamma}(\boldsymbol{r} - \boldsymbol{r}')\, dV' dV
\end{aligned}
\tag{10}
$$

2.3 Multi-site (MS) Mori-Tanaka (MT) scheme formulation

Mori–Tanaka (MT) formulation (Ferrari, 1991) is a homogenisation model built on the concept of Eshelby's dilute model (Eshelby, 1957). The MT scheme considers the matrix phase to be the reference medium ($\boldsymbol{c}^{o} = \boldsymbol{c}^{R}$) and the average strain field inside the matrix is approximated by the strain within the reference medium ($\varepsilon^{o} \cong \mathbf{E}^{R}$). The MT scheme allows us to introduce kinematic equation without the unknown tensors $\boldsymbol{T}^{oo}$and $\boldsymbol{T}^{Io}$. This leads to $\varepsilon^{o} \cong \mathbf{E}^{o}$, with $\mathbf{E}^{o}$ being the strain of an RVE having the matrix properties. Therefore, one gets:

$$\zeta^o = \mathbf{I}\,, \qquad \mathfrak{z}^o = \mathbf{0} \tag{11}$$

The localisation tensors ζ^I and $\mathfrak{z}^I$ of the remaining constituents of the RVE are computed through an iterative process as introduced above:

$$\begin{cases} \zeta^{\boldsymbol{I}}_{(0)} = \left(\mathbf{I} + \boldsymbol{T}^{II} : (\boldsymbol{c}^I - \boldsymbol{c}^o)\right)^{-1} \\ \mathfrak{z}^I_{(0)} = \zeta^I_{(0)} : \boldsymbol{T}^{II} : \Delta\boldsymbol{\beta}^I \\ \zeta^{\boldsymbol{I}}_{(i+1)} = \left(\mathbf{I} + \boldsymbol{T}^{II} : (\boldsymbol{c}^I - \boldsymbol{c}^o)\right)^{-1} : \left(\mathbf{I} - \sum_{\substack{J=1 \\ J\neq I}}^{N} \boldsymbol{T}^{IJ} : (\boldsymbol{c}^J - \boldsymbol{c}^o) : \zeta^J_{(i)}\right) \\ \mathfrak{z}^{\boldsymbol{I}}_{(i+1)} = (\mathbf{I} + \boldsymbol{T}^{II} : (\boldsymbol{c}^I - \boldsymbol{c}^o))^{-1} : \left[\boldsymbol{T}^{II} : \Delta\boldsymbol{\beta}^I + \sum_{\substack{J=1 \\ J\neq I}}^{N} \boldsymbol{T}^{IJ} : \left(\Delta\boldsymbol{\beta}^J - (\boldsymbol{c}^J - \boldsymbol{c}^o) : \mathfrak{z}^J_{(i)}\right)\right] \\ I = 1, 2, \dots, N \end{cases} \tag{12}$$

Taking advantage of the first expression in Eq.(8), the unknown global strain concentrations are given by:

$$\begin{cases} \boldsymbol{A}^o = \zeta^o : (\overline{\zeta}^I)^{-1} = [\mathrm{v}_o \mathbf{I} - \sum_{I=1}^{N} \mathrm{v}_I (\mathbf{I} - \zeta^I)]^{-1} \\ \boldsymbol{a}^o = \mathfrak{z}^o - \boldsymbol{A}^o : \overline{\mathfrak{z}}^I = -\boldsymbol{A}^o : \sum_{I=1}^{N} \mathrm{v}_I\, \mathfrak{z}^I \\ \boldsymbol{A}^I = \zeta^I : \boldsymbol{A}^o \\ \boldsymbol{a}^I = \mathfrak{z}^I - \boldsymbol{A}^I : \overline{\mathfrak{z}}^I = \mathfrak{z}^I + \zeta^I : \boldsymbol{a}^o \\ I = 1, 2, \dots, N \end{cases} \tag{13}$$

Finally, by using the discrete form of Eqs. (3) and (4), the effective properties of the composite material are then deduced from the following relations:

$$\begin{cases} \boldsymbol{C}^{MMT} = \sum_{I=0}^{N} \mathbf{v}_I \boldsymbol{c}^I : \boldsymbol{A}^I = \boldsymbol{c}^o + \sum_{I=1}^{N} \mathbf{v}_I (\boldsymbol{c}^I - \boldsymbol{c}^o) : \boldsymbol{A}^I \\ \boldsymbol{\beta}^{MMT} = \sum_{I=0}^{N} \mathbf{v}_I [\boldsymbol{\beta}^I - (\boldsymbol{c}^I - \boldsymbol{c}^o) : \boldsymbol{a}^I] = \boldsymbol{\beta}^o + \sum_{I=1}^{N} \mathbf{v}_I [(\Delta\boldsymbol{\beta}^I) - (\boldsymbol{c}^I - \boldsymbol{c}^o) : \boldsymbol{a}^I] \\ \boldsymbol{\alpha}^{MMT} = (\boldsymbol{C}^{MMT})^{-1} : \boldsymbol{\beta}^{MMT} \end{cases} \quad (14)$$

where the superscript *MMT* states for Multi-site Mori–Tanaka approximation of overall properties.

When a composite material consists of an isotropic matrix and aligned, isotropic inclusions, its effective elastic properties become transversely isotropic. Following (Doghri and Ouaar, 2003; Torquato, 1997; Torquato, 2002), any anisotropic fourth-order tensor $\mathbb{\Gamma}^{\mathrm{ani}}$, could be averaged into an isotropic operator $\mathbb{\Gamma}^{\mathrm{iso}}$ where:

$$\begin{aligned} \mathbb{\Gamma}_{ijkl}^{iso} = & \left(\frac{1}{3}\mathbb{\Gamma}_{iijj}^{ani}\right)\left(\frac{1}{3}\delta_{ij}\delta_{kl}\right) \\ & + \frac{1}{5}\left(\mathbb{\Gamma}_{ijji}^{ani} - \frac{1}{3}\mathbb{\Gamma}_{iijj}^{ani}\right)\left(\frac{1}{2}(\delta_{ik}\delta_{jl} + \delta_{il}\delta_{jk}) - \frac{1}{3}\delta_{ij}\delta_{kl}\right) \end{aligned} \quad (15)$$

where δ is the Kronecker's delta. Application of Eq. (15) on $\boldsymbol{C}^{MMT}$ results in obtaining isotropic stiffness tensor of randomly-oriented inclusion composite at the macroscale. Moreover, in order to compute the isotropic part Γ_{ij}^{iso} of a second-order tensor representing the effective thermal properties:

$$\Gamma_{ij}^{iso} = \frac{1}{3}\Gamma_{ii}^{ani}\delta_{ij} \quad (16)$$

It should be noted that, in the case of the classical One-site (OS) version, the interactions among inclusion $\boldsymbol{I}$ and its neighbours $\boldsymbol{J}$ are neglected, i.e. all the $\boldsymbol{T}^{IJ}$ tensors vanish. One-site

interaction modelling provides accurate predictions in the case of random microstructure (Fassi-Fehri and A. Hihi, 1989; Kroner, 1980). In this case, the calculation of localised concentration tensors are explicit given by:

$$\begin{cases} \zeta^{\boldsymbol{I}} = \left(\mathbf{I} + \boldsymbol{T}^{II} : (\boldsymbol{c}^{I} - \boldsymbol{c}^{o})\right)^{-1} \\ \mathfrak{Z}^{\boldsymbol{I}} = (\mathbf{I} + \boldsymbol{T}^{II} : (\boldsymbol{c}^{I} - \boldsymbol{c}^{o}))^{-1} : (\boldsymbol{T}^{II} : \Delta\boldsymbol{\beta}^{I}) \\ I = 1, 2, \dots, N \end{cases} \tag{17}$$

2.4 Aligned microstructure topology

The topology of the considered ordered or aligned microstructure consists of a group of eight ellipsoidal inclusions fashioning a cubic unit structure within the matrix phase, as shown in Figure 1(a). The semi-axes (a, b, c) of ellipsoidal inclusions are given in terms of two morphological parameters $K_1 = \frac{b}{a}$ and $K_2 = \frac{c}{a}$. An additional topological parameter $\delta = \frac{\mathbf{d}}{a}$ is presented to characterise the description of inclusions' neighbourhood, where **d** is the distance separating each inclusion from one another (Azoti et al., 2015; Kpobie et al., 2012). The volume fraction of inclusions v_f would be:

$$\mathrm{v}_f = \frac{f}{V_c} = \frac{4\pi k_1 k_2}{3(\delta + 2)(\delta + 2k_1)(\delta + 2k_2)} \tag{18}$$

where $f = \frac{4\pi abc}{3}$ is the inclusion volume and V_c is the volume of the considered unit cell. Inclusions interpenetration occurs at the percolation threshold $\mathrm{v}_{f_{threshold}} = \frac{\pi}{6}$ at $\delta = 0$. Graphene platelets (GPLs) will be considered as ellipsoidal inclusions having a circular cross-section $(K_1 = 1)$ with an aspect ratio (*AR*) = K_2. The essential variable parameter δ influencing the global response through the volume fraction is computed from the cubic equation:

$$\delta^3 + (4 + 2k_2)\delta^2 + (8k_2 + 4)\delta + \left((24v_f - 4\pi)/3v_f\right)k_2 = 0.0 \tag{19}$$

the cube dimensions $L, h,$ and l (Figure 1(b)) characterise six neighbours located on three orthogonal planes passing by the centre of the reference inclusion, where:

$$L = a(\delta + 2), \qquad h = a(\delta + 2k_2), \qquad l = a(\delta + 2k_1) \tag{20}$$

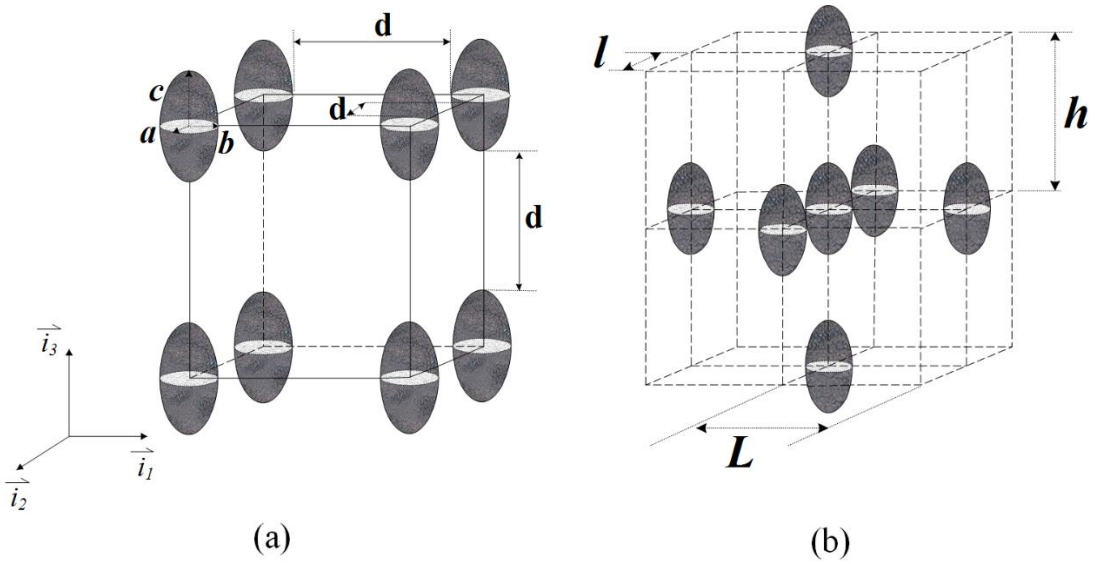

Figure 1 *Lattice arrangement of ellipsoidal inclusions:* (a) *cubic unit cell and* (b) *ellipsoidal inclusion (the one in the middle) interacting with six neighbour inclusions (Azoti et al., 2015).*

Figure 2 shows the evolution of the topological parameter δ versus the volume fraction $\mathbf{v}_f$ for different values of the aspect ratio (AR) in the case of ellipsoidal inclusions having a circular cross-section, $(K_1 = 1)$. The distance between inclusions decreases as the volume increases. The highest values are obtained as the shape of the inclusions tend towards prolate morphology, whereas oblate inclusions, for instance, AR=10^{-3}, account for very small volume fractions. Therefore, the volume fraction controls the parameter δ. The parameter δ influences the global response; it represents an essential variable in the multi-site modelling since it characterizes the distance in the description of the inclusions' neighbourhood.

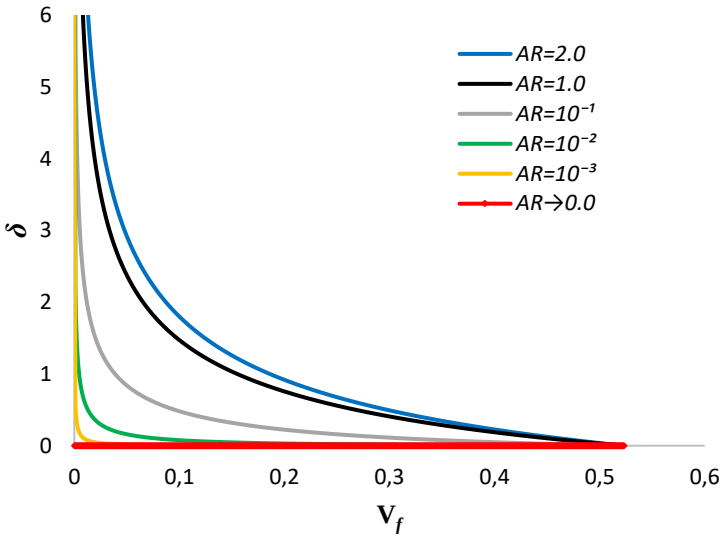

Figure 2 *Volume fraction* $\mathbf{V}_f$ *versus topological parameter* $\boldsymbol{\delta}$.

The flow-chart shown in Figure 3 describes the developed algorithm to compute tensors of $\boldsymbol{C}^{MMT}$, $\boldsymbol{\alpha}^{MMT}$, $\boldsymbol{C}_{iso}^{MMT}$ and $\boldsymbol{\alpha}_{iso}^{MMT}$ defining equivalent thermo-elastic properties using the localisation tensors ζ^I and $\mathfrak{z}^I$ and the global strain concentration tensors $\mathbf{A}^I$ and $\boldsymbol{a}^I$ representing Ith phase of the composite materials.

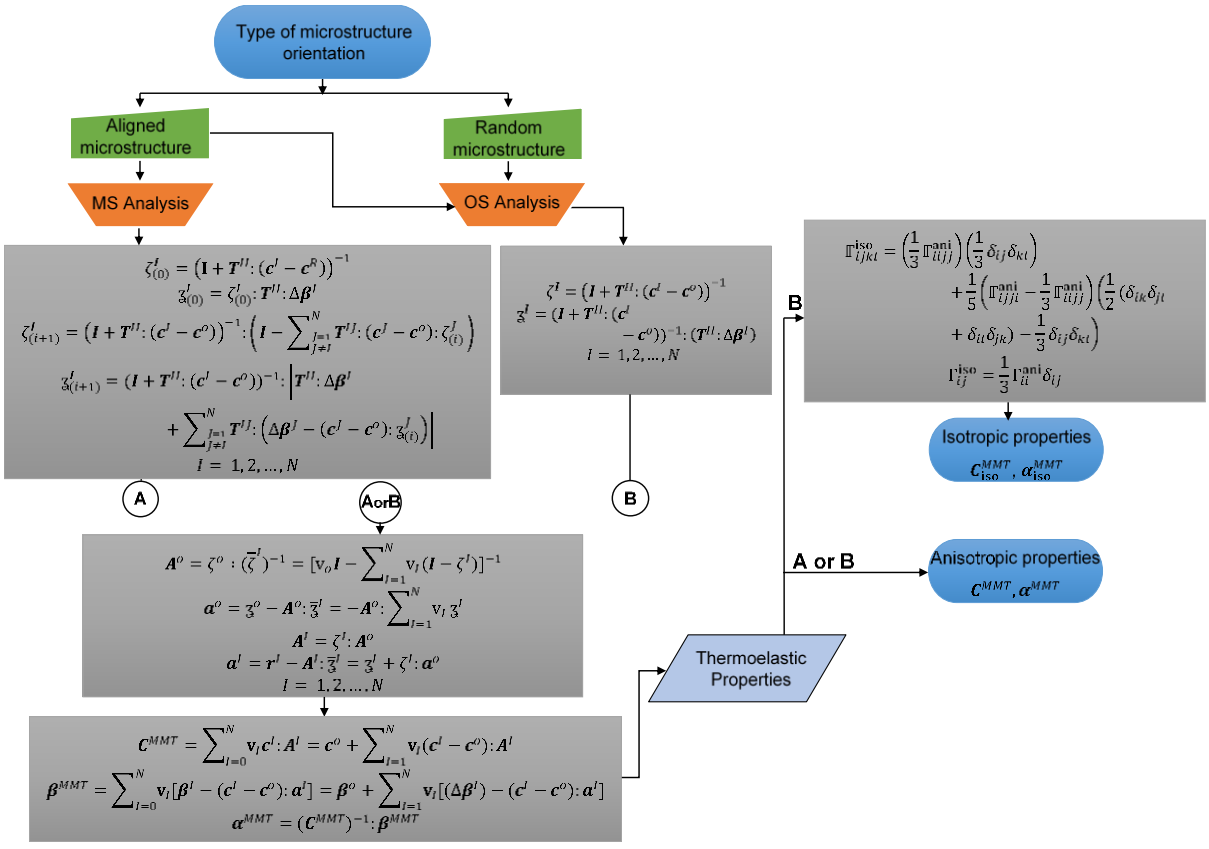

Figure 3 Flow chart showing the algorithm of analysis methodology.

3 Finite element modelling (FEM)

For graphene platelet (GPL)-reinforced polymer PA6 composite materials (Table 1), a 3D finite element modelling (FEM) is considered under the software Abaqus (DassaultSystèmes, 2014). The microstructure is defined conformally to the analytical formulation. The design parameters studied herein are the aspect ratio (AR) and the volume fraction. Eventually, the orientation of the GPL is accounted for within the analysis.

Table 1 *Material properties for GPL/PA6 composite materials considered for the current study.*

	Polyamide-Nylon 6 (PA6)	GPL
Young's modulus (GPa)	2.0	10^3
Poisson's ratio	0.39	0.22
CTE (10^{-6}/K)	95 (2020a; 2020b; Gaitonde et al., 2010)	2.9 (Sadowski et al., 2015)

The RVE is then generated using a plugin of Digimat FE software (MSC, 2016), as shown in Figure 4. First-order tetrahedral elements C3D4 are used with very fine meshing. In addition, periodic boundary conditions are defined for the RVE, which is submitted to a thermomechanical loading. Indeed, this loading is composed of a static step analysis (uniaxial and shear loading) along with a predefined temperature field. To ensure the periodic boundary conditions, equations constraints are deployed in Abaqus to constraints the faces of the RVE one another. Figure 5 and Figure 6 give an overview of the equations constraints and the applied temperature fields.

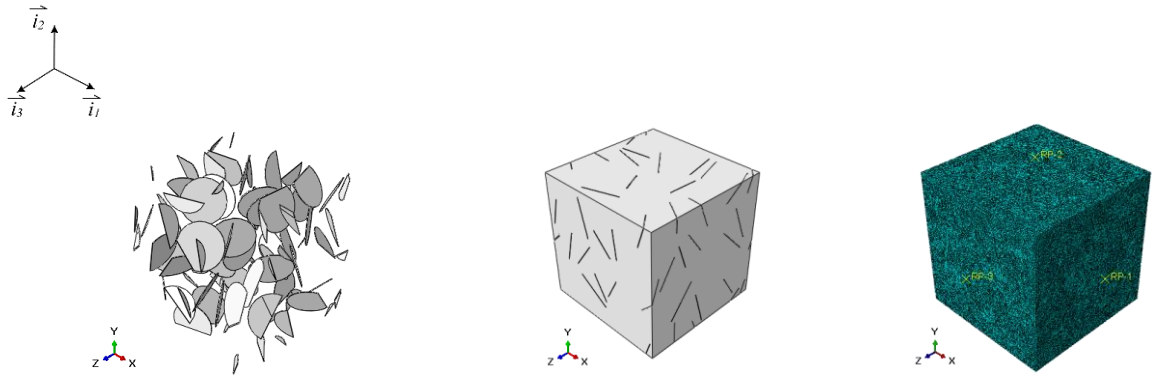

(a) (b) (c)

Figure 4 *Randomly-oriented GPL reinforced RVE for AR=10^{-2} and* v_f *=0.01:* (a) *graphene platelets,* (b) *numerical model, and* (c) *C3D4 meshing.*

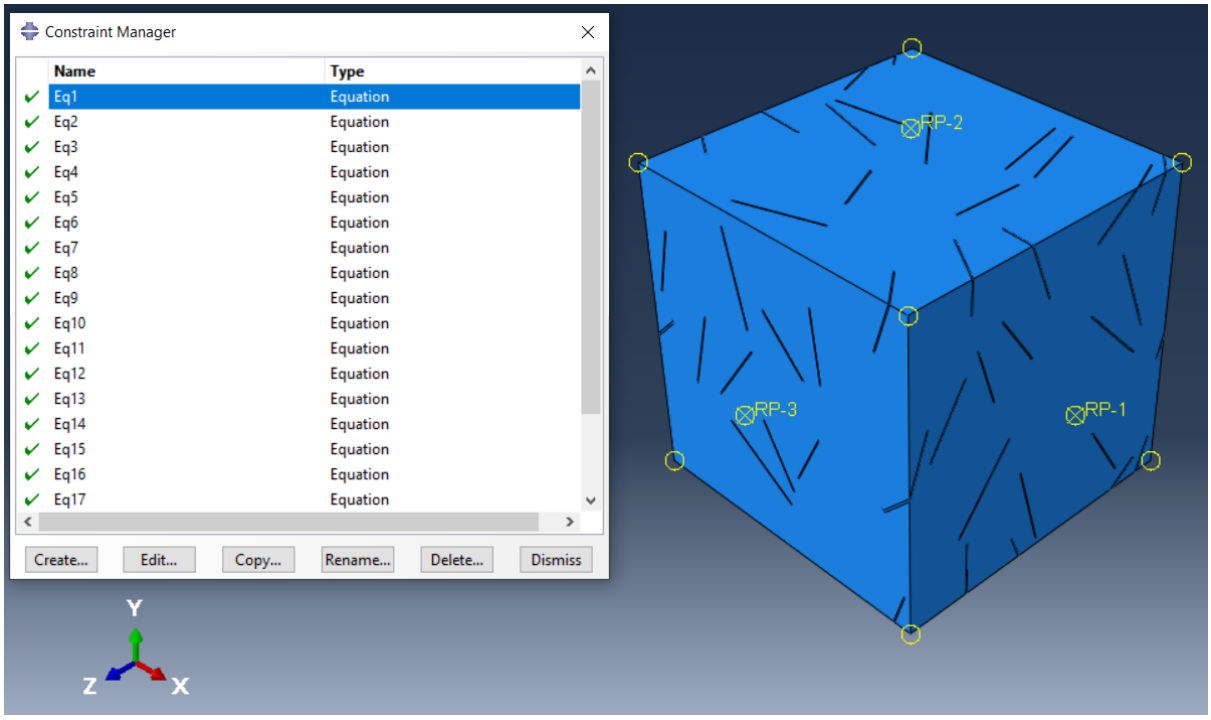

Figure 5 *Equation constraints ensuring the periodic boundary conditions on the RVE*

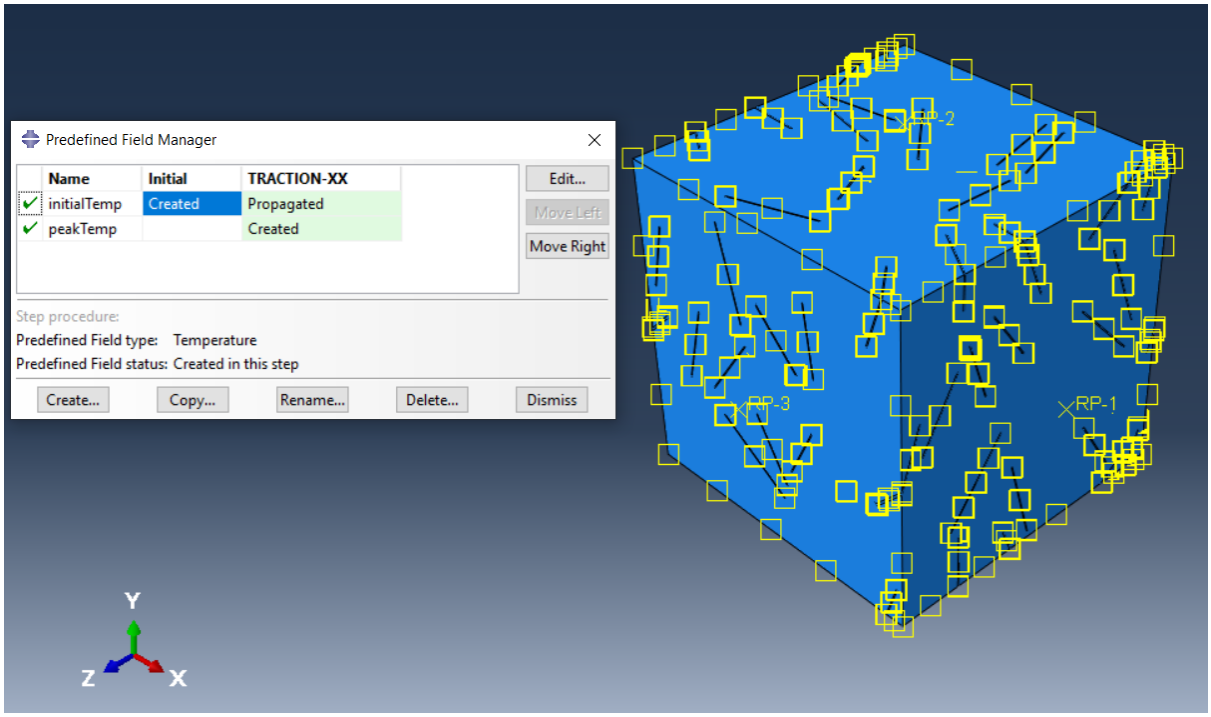

Figure 6 *Illustration of a predefined temperature field on the RVE*

The determination of the thermomechanical effective properites is performed through a post-processing using Python script along with the Abaqus Output data base ODB. For such a purpose, the fieldoutputs, for instance the stress [S], the strain [E], the temperature [TEMP]

and the thermal strain [THE] as well as the volume of Guass integration points [IVOL] are extracted for both the matrix and the inclusions of the composite as shown in Appendix A. The implementation of the average field outputs within the matrix (or the inclusions) involves the mean value of these field outputs over the total volume of the integrations points. For example, the computation of the average stress within the matrix phase is given, such as:

$$AVE\_S\_M = \frac{\sum_{i=1}^{N_M} IVOL[i] \times S[i]}{\left(\sum_{i=1}^{N_M} IVOL[i] + \sum_{j=1}^{N_I} IVOL[j]\right)} \tag{21}$$

with N_M denoting the number of Gauss integration points within the matrix and N_I that of the inclusions. From a similar approach, one can have the average stress within the inclusions such as:

$$AVE\_S\_I = \frac{\sum_{i=1}^{N_I} IVOL[i] \times S[i]}{\left(\sum_{i=1}^{N_M} IVOL[i] + \sum_{j=1}^{N_I} IVOL[j]\right)} \tag{22}$$

The macroscopic stress within the composite is therefore obtained by:

$$S\_MACRO = AVE\_S\_M + AVE\_S\_I \tag{23}$$

From a similar approach, one can have the macroscopic strain within the composite such as:

$$E\_MACRO = AVE\_E\_M + AVE\_E\_I \tag{24}$$

The macroscopic thermal strain inside the composite is given by:

$$THE\_MACRO = AVE\_THE\_M + AVE\_THE\_I \tag{25}$$

The macroscopic temperature field applied to the composite yields:

$$TEMP\_MACRO = AVE\_TEMP\_M + AVE\_TEMP\_I \tag{26}$$

Under a uniaxial load for instance a TRACTION-11, and using Python (x,y) array indexing, the engineering coefficients are obtained such as:

$$E_{11} = \frac{\sigma_{11}}{\varepsilon_{11}} = \frac{S\_MACRO[0,0]}{E\_MACRO[0,0]} \tag{27}$$

$$v_{12} = -\frac{\varepsilon_{22}}{\varepsilon_{11}} = -\left(\frac{E\_MACRO[[1,1]]}{E\_MACRO[0,0]}\right) \tag{28}$$

$$v_{13} = -\frac{\varepsilon_{33}}{\varepsilon_{11}} = -\left(\frac{E\_MACRO[2,2]}{E\_MACRO[0,0]}\right) \tag{29}$$

$$\alpha_{11} = \frac{\varepsilon_{11}^{T}}{\Delta T} = \left(\frac{THE\_MACRO[0,0]}{TEMP\_MACRO}\right) \tag{30}$$

Under a shear load for instance a SHEAR-12 one has for the engineering coefficients:

$$\mu_{12} = \frac{1}{2}\left(\frac{\sigma_{12}}{\varepsilon_{12} + \varepsilon_{21}}\right) = \frac{1}{2}\left(\frac{S\_MACRO[0,1]}{E\_MACRO[0,1] + E\_MACRO[1,0]}\right) \tag{31}$$

The post-processing of the RVE, which enables the computation of engineering coefficients is shown in the Appendix A.

4 Models validation

Model validation is established to demonstrate the capability of the current models to reproduce results from the general literature. One-site (OS) scheme is mainly used to model randomly-oriented inclusions composite, as has been shown by Kröner (Kroner, 1980; Kröner, 1977) that the effective properties based on OS approach would be precise in the case of perfect disorder in random media. In comparison, Multi-site (MS) is only used to model composites with aligned inclusions. There is no need for MS in the case of randomly distributed inclusions as more computational cost and time can be underlined to obtain the effective properties depending on the selected parameters. The OS approach has also been used to model aligned inclusion composites for comparison purposes.

The model predictions are compared with the works by Sadowski et al. (2015). The material properties used for analyses are presented in Table 2 and Table 3. Figure 7 illustrates the influence of two different graphite geometries represented by aspect ratios (ARs) on randomly-oriented graphite copper-matrix composite. Figure 8 reveals the behaviour of randomly-oriented graphene copper-matrix composite when the AR tends to zero. Different trends are obtained for the Young's moduli and the coefficient of thermal expansion. Indeed, the higher the volume fraction, the lower the Young's moduli (E_{eff}/E_o) of graphite composite (Figure 7 (a), (b)). The decrease in the Young's moduli values is explained by the low contrast between the graphite and the copper in terms of stiffness. However, for the graphene which exhibits a high contrast of stiffness with respect to the copper, it is observed an increase in the mechanical response with the volume fraction as shown in Figure 8 (a).

Besides, the effective coefficient of thermal expansion (CTE) (α_{eff}/α_o) shows an unusual non-monotonic behaviour. Indeed, a parabolic evolution is observed for graphite composite, as shown in Figure 7 (c), (d). This unexpected evolution was initially obtained by Rouby (2005) and later reproduced by Kpobie et al. (2012) for the transverse CTE of glass fibres reinforced epoxy-matrix. An explanation of this trend comes from the nonlinear dependence of the effective CTE regards to the volume fraction trough the Eq. (14) Indeed, Rouby (2005) derived the effective longitudinal (α_{11}) and transversal (α_{33}) CTE for unidirectional fibres composites. He showed that the transversal CTE undergoes a parabolic trend versus the volume fraction. In addition, for a random microstructure, he showed that the effective CTE is a combination of transversal and longitudinal expressions of CTE leading to a nonlinear behaviour versus the volume fraction. Due to the high contrast properties between the graphene and the copper matrix, a decreasing trend for the CTE is observed in Figure 8 (b). Although parabolic behaviour is noticed, this behaviour remains coherent with the literature data.
Concerning aligned microstructures, Figure 9 presents a comparison between the present model versus the axial and transversal thermoelastic moduli by Sadowski et al. (2015). The effective elastic moduli are well predicted by the present model in Figure 9 (a) and (b), while some discrepancy can be noticed for the effective coefficient of thermal expansion due to the nonlinear behaviour explained above.

Regards to the FE modelling, numerical results indicate satisfactory results versus the literature results for both effective Young's moduli and coefficient of thermal expansion. Good

agreement is found between the present analytical predictions and FE modelling with respect to results by Sadowski et al. (2015) in terms of Young's moduli.

In addition, CTE behaviour was also compared to works by Shi et al. (2016) as depicted in Figure 10 using material properties in Table 4. Current model predictions of the longitudinal effective(α_{11}/α_o) for both OS and MS approaches coincide with Shi's results, while the transversal effective (α_{33}/α_o) follows the parabolic behaviour elucidated by Rouby (2005).

Table 2 *Material properties for isotropic polycrystalline graphite (Gt) and isotropic copper matrix (Cu), Sadowski et al. (2015).*

	Gt	Cu
Young's modulus (GPa)	10.0	120
Poisson's ratio	0.16	0.34
CTE (10^{-6}/K)	2.9	17.0

Table 3 *Material properties for isotropic graphene (Gn) and isotropic copper matrix (Cu), Sadowski et al. (2015).*

	Gn	Cu
Young's modulus (GPa)	1025	120
Poisson's ratio	0.16	0.34
CTE (10^{-6}/K)	-8.0	17.0

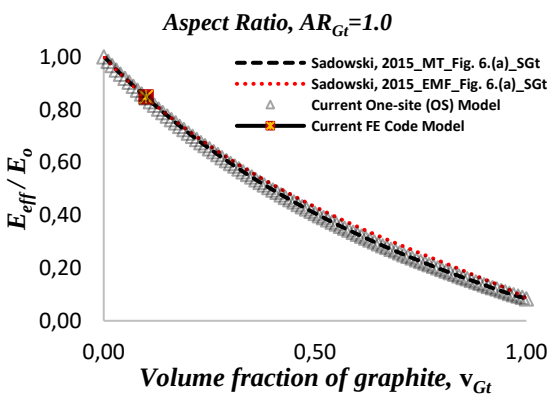

(a)

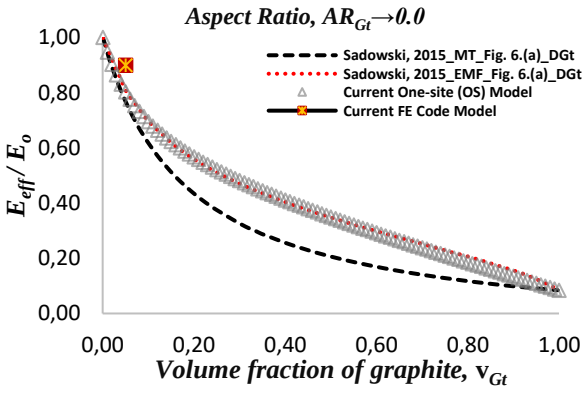

(b)

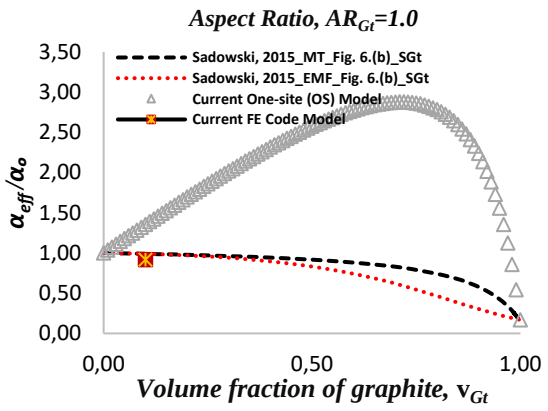

(c)

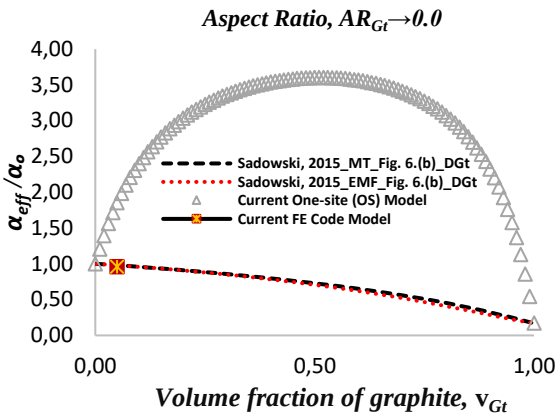

(d)

Figure 7 *Randomly-oriented graphite copper-matrix composite: influence of the graphite shape AR on* (a) *and* (b) *effective Young's modulus,* (c) *and* (d) *coefficient of thermal expansion.*

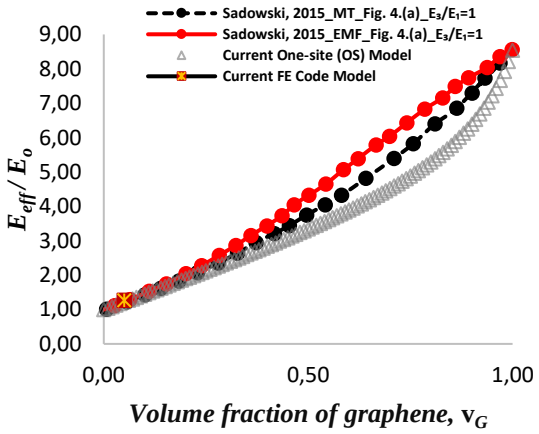

(a)

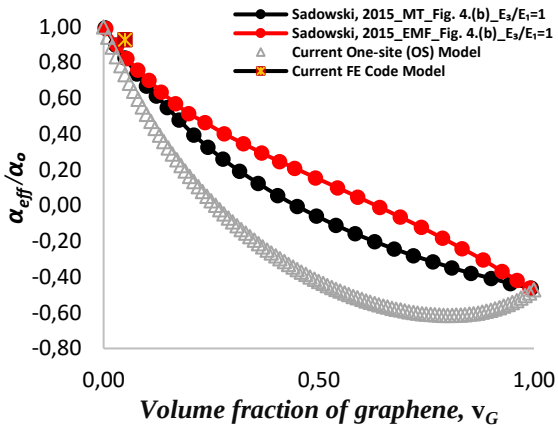

(b)

Figure 8 *Randomly-oriented graphene copper-matrix composite:* (a) *effective Young's modulus and* (b) *coefficient of thermal expansion, with* $AR_G \rightarrow 0.0$.

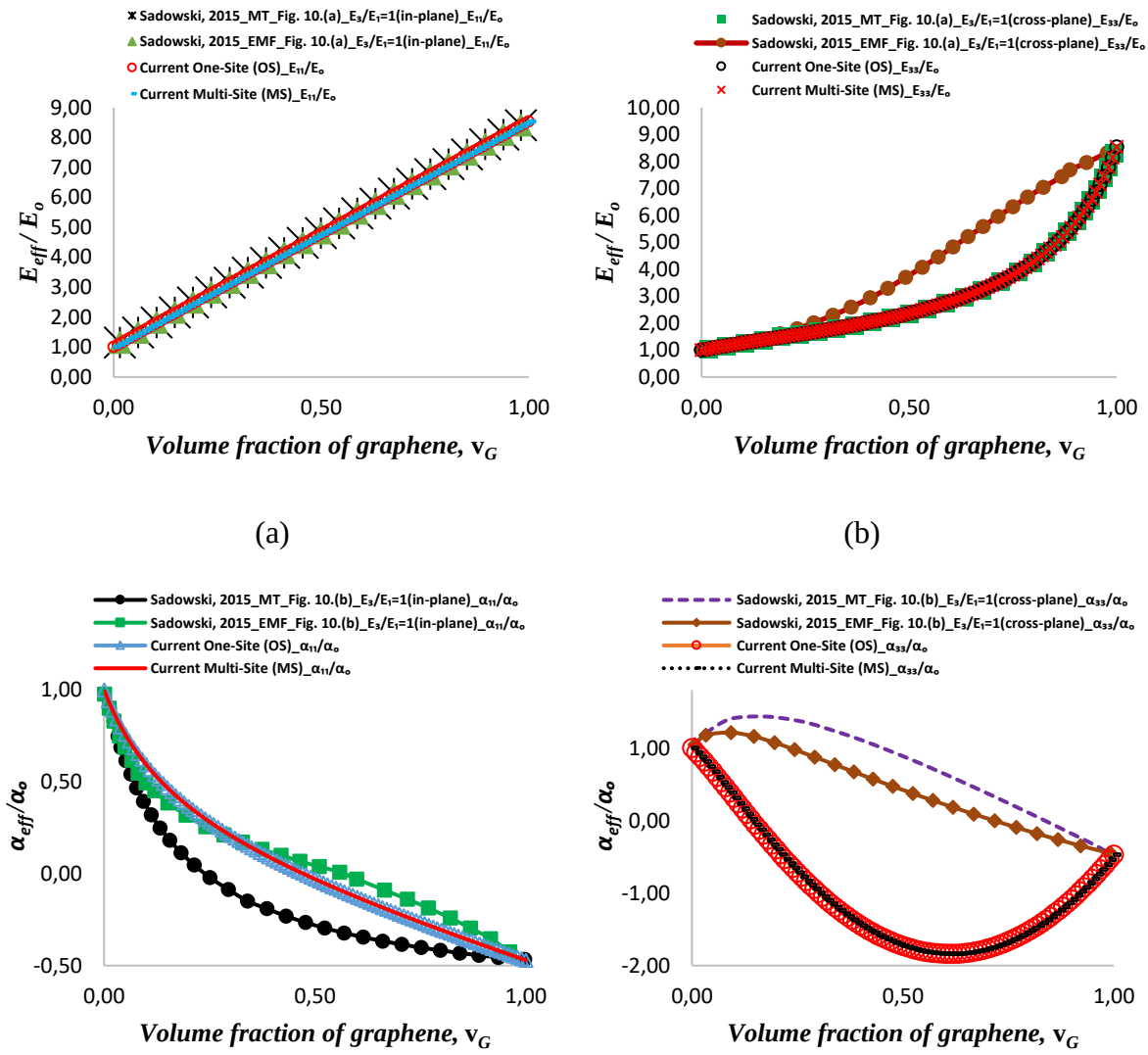

Figure 9 *Aligned graphene copper-matrix composite:* (a) *and* (b) *effective Young's modulus,* (c) *and* (d) *coefficient of thermal expansion, with* $AR_G \rightarrow 0.0$.

Table 4 *Properties of graphene inclusions (GPs) and epoxy, Shi et al. (2016).*

	GP	Epoxy
Young's modulus (GPa)	1060	2.76
Poisson's ratio	0.006	0.35
CTE (10^{-6}/K)	7.83	81

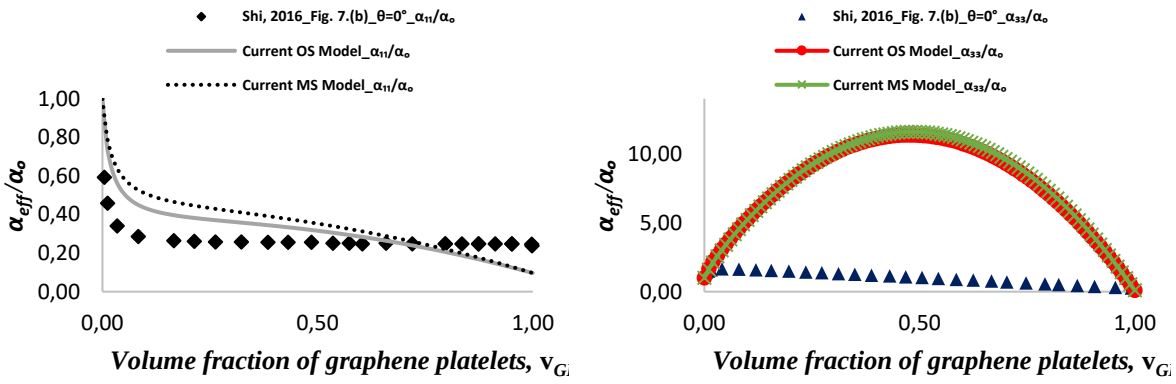

(a) (b)

Figure 10 *Coefficient of thermal expansion of aligned graphene platelets epoxy-matrix composite with* AR_{GP}*=0.001.*

In summary, the present modelling gives correct prediction of the mechanical properties in terms of Young's modulus in both its OS and MS versions. Regarding the CTE, it takes into account a non-linear variation of the CTE initially described in the works by Rouby (2005) for the transversal CTE and later by Kpobie et al. (2012). As a result, the predictions remain different with respect to the MT and EMF mean-field approaches by Sadowski et al. (2015).

In addition, it is found in Figure 9 and Figure 10 that the anisotropy due to the spatial distribution had a small variation on the CTE. This means that both OS and MS models predict close or same CTE. This behaviour, also observed by Kpobie et al. (2012), is similar to evolution mainly due to the volume fraction.

The difference between the OS model and the MS model lies in the fact that the latter, in addition to taking into account the interaction between the inclusion and the matrix, allows for a better description of the anisotropy by taking into account the neighbourhood of the inclusion i.e. its topological texture (spatial distribution and orientation).

5 Results and discussions

The graphene platelets (GPLs) reinforced PA-6 polymer matrix composite with material properties presented in Table 1 has been considered for the current study. Although graphene hexagonal lattice permits the display of anisotropic behaviour (Azoti and Elmarakbi, 2017; Shokrieh et al., 2014), the dominant mechanical properties of graphene remain the in-plane behaviour which has been demonstrated to exhibit isotropic elastic behaviour (Cho et al., 2007; Lee et al., 2008). Based on current modelling, isotropic behaviour of GPLs and PA-6 matrix

are considered. The effective response of the composite under investigation may be fully described and assessed through two parameters: the platelets aspect ratio (AR) and the volume fraction v_f.

5.1 Analytical results

5.1.1 *Randomly-oriented microstructure*

Analytical One-site (OS) approach has been used to model randomly-oriented GPL/PA6 composite. Figure 11 presents the results of the selected design parameters. Based on current results, it can be seen that as the inclusion geometry tends towards disk-like shape (i.e. as the aspect ratio decreases) under a selected v_f, an increase is manifested in shear and Young's moduli. On the contrary, Poisson's ratio and coefficient of thermal expansion (CTE) suffer a reduction. Except for CTE, v_f has a similar effect on the properties for a selected AR. One can notice that prior to AR=10^{-2}, CTE increases with increasing v_f.

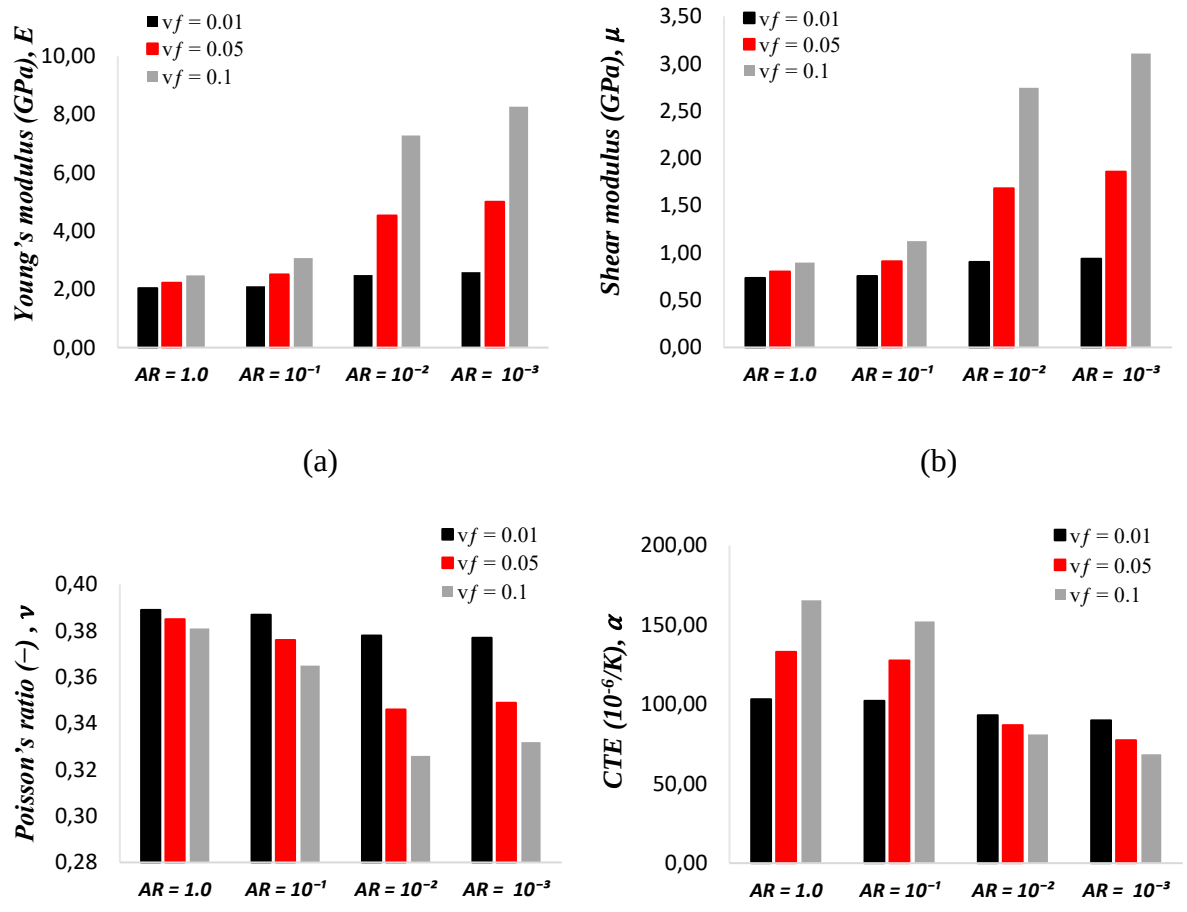

Figure 11 *Analytical OS results for randomly-oriented inclusions GPL/PA6 composite.*

5.1.2 *Aligned inclusions (ordered microstructure)*

One-site (OS) and Multi-site (MS) techniques were exploited to model the behaviour of aligned GPL/PA-6 composite material. Results are reported in Figure 12. In contrast to CTE, along with Poisson's ratio, shear and Young's moduli values recorded for OS are higher than their counterparts for MS.

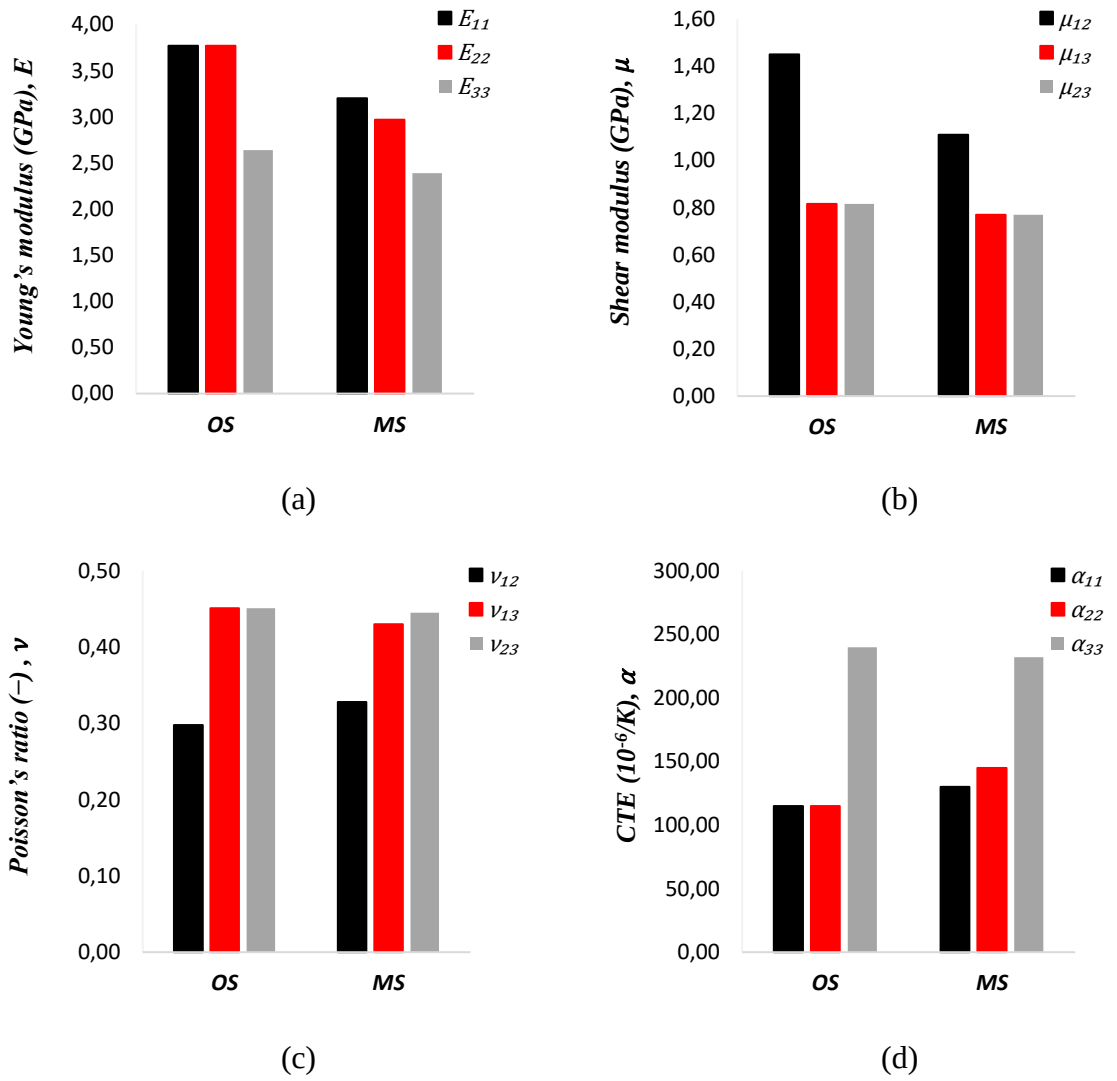

Figure 12 *Analytical OS and MS results for aligned inclusions GPL/PA6 composite of* $AR=10^{-1}$ *and* $v_f=0.1$.

Results in Figure 13 compare the effective OS and MS thermoelastic behaviour of the GPL/PA-6 composite. Figure 13 (a) depicts the evolution of the normalised axial (E_{11}/E_o) and transverse (E_{33}/E_o) Young's moduli versus the volume fraction of graphene. This figure shows an increasing monotonic trend of the reinforcement of the mechanical stiffness with the

volume fraction. The difference between the OS and MS predictions resides in the choice of the inclusion's neighbourhood. Also, a small bounce is observed for the axial (E_{11}/E_o) at very small volume fraction. This behaviour just results in numerical instabilities. Figure 13 (b) describes the evolution of effective axial (α_{11}/α_o) and transverse (α_{33}/α_o). A coherent trend is found between predictions with respect to the developed micromechanics formulations.

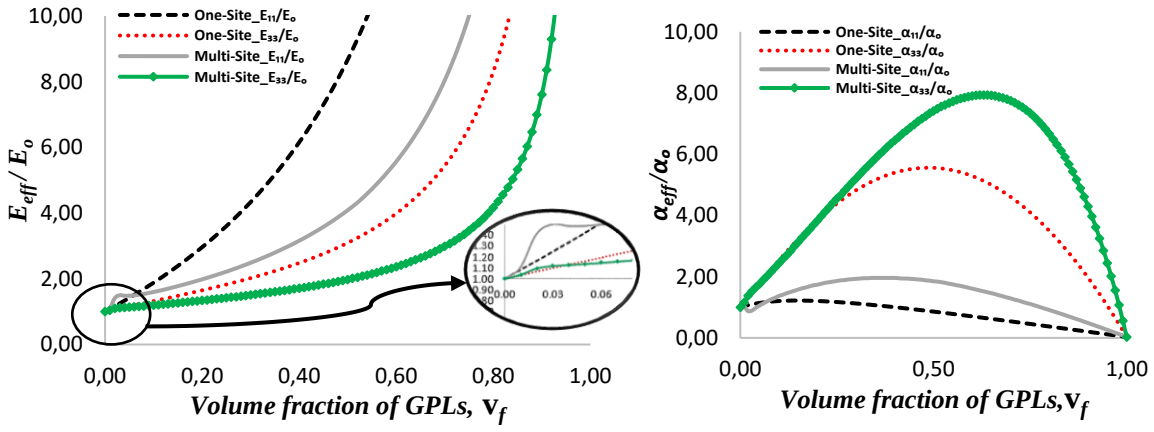

(a) (b)

Figure 13 *Influence of OS and MS ordered microstructure schemes on* (a) *and* (b) *effective Young's modulus,* (c) *and* (d) *coefficient of thermal expansion with AR=0.1.*

5.2 Numerical results

A series of FEA analysis were conducted on the RVE using Abaqus and compared against the analytical modelling approach presented in the previous section. Due to the small size of inclusions (AR < 10^{-2}) requiring minuscule discretization levels, mesh generation is very intricate. As a result, the lowest value of the aspect ratio used for numerical analysis is AR= 10^{-2}.

5.2.1 *Random inclusion order*

FE numerical results of the RVE for randomly-oriented inclusions microstructure are presented in Figure 14 and compared with the analytical OS results. In both cases, interactions with the neighbourhood are not accounted for.

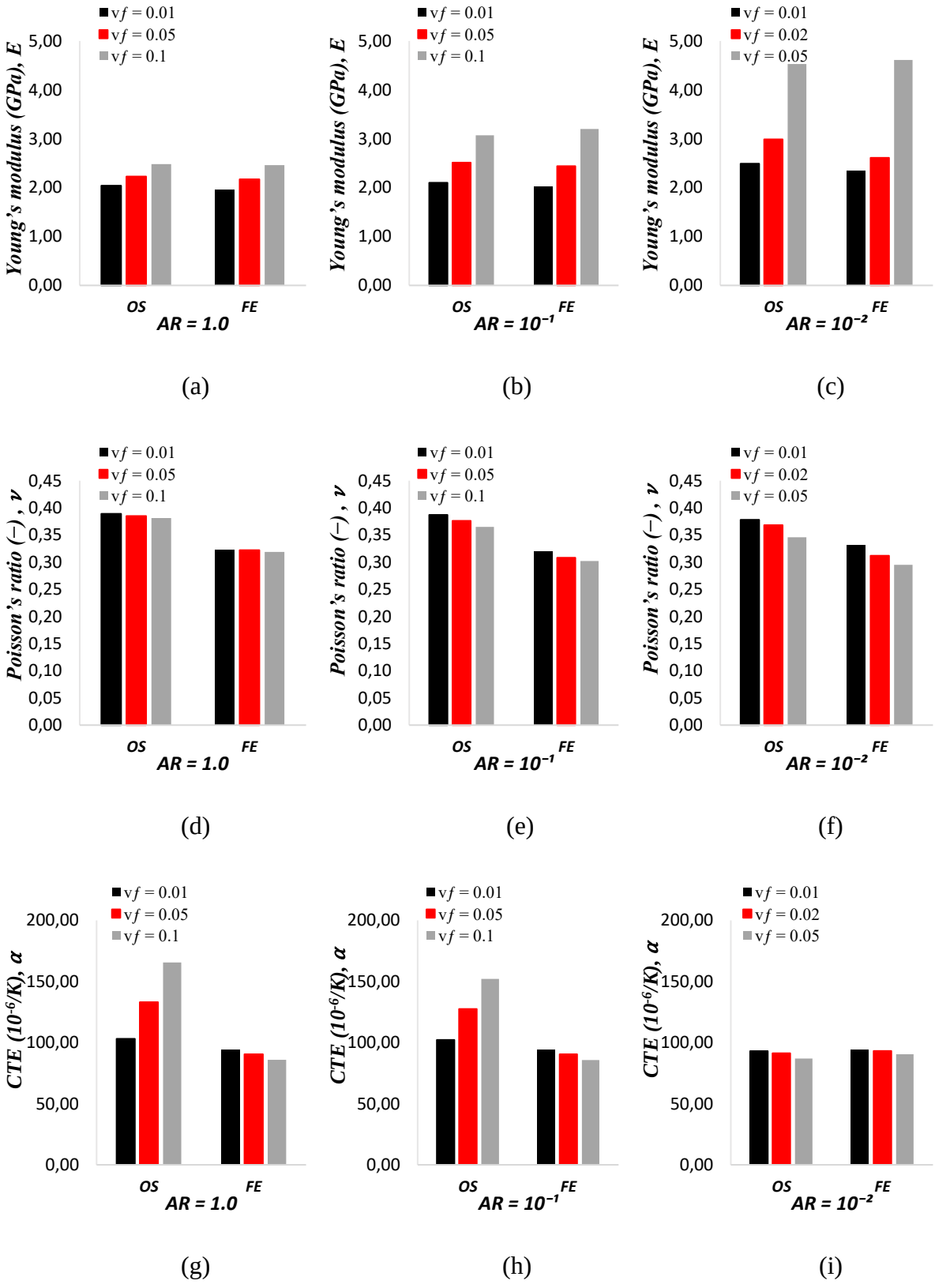

Figure 14 *Comparison between analytical OS and numerical results for randomly-oriented inclusions GPL/PA6 composite.*

Results in Figure 14 indicate a good agreement between the numerical Young's moduli and the analytical OS ones (Figure 14 (a) – (c)). Poisson's ratios tend to be lower in the FE case compared to the OS model (Figure 14 (d) – (f)). In terms of FE effective CTE (Figure 14 ((g) – (i)), the volume fraction has a critical influence on the overall behaviour. The CTE decreases monotonously when the volume fraction increases. The aspect ratio influence is minor herein since not much significant difference is noticed between the CTE for the selected aspect ratio.

A closer agreement is obtained between both analytical OS and FE results at AR=10^{-2} specifically for CTE. The contour plots of Mises stress and the strain deformation within the GPLs and the PA6-matrix are depicted in Figure 15 and Figure 16, while the thermal strain is shown in Figure 17 for two different aspect ratio.

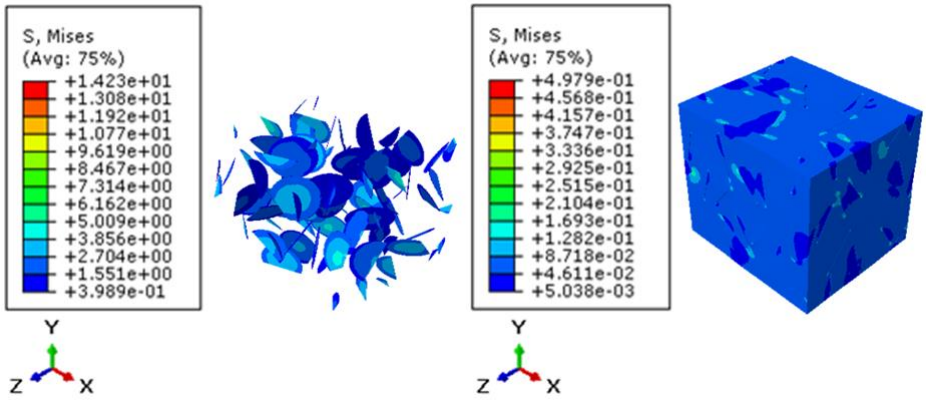

(a)

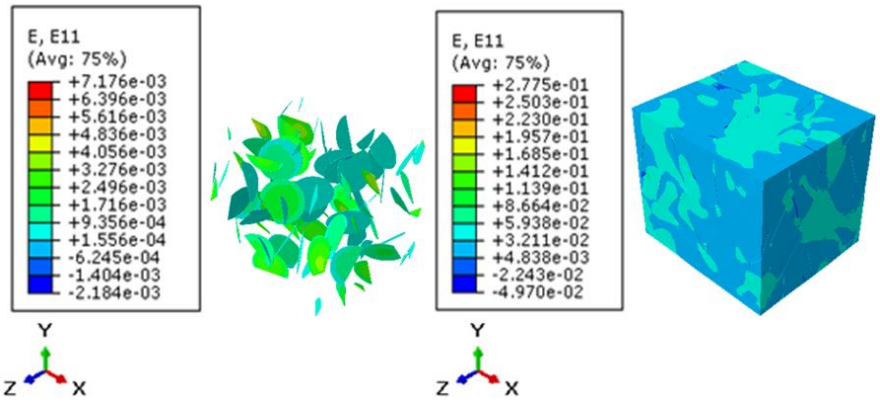

(b)

Figure 15 *Illustration of contour plots for for AR=10^{-2}* and v_f *=0.01:* (a) *Mises stress* (b) *uniaxial strain*

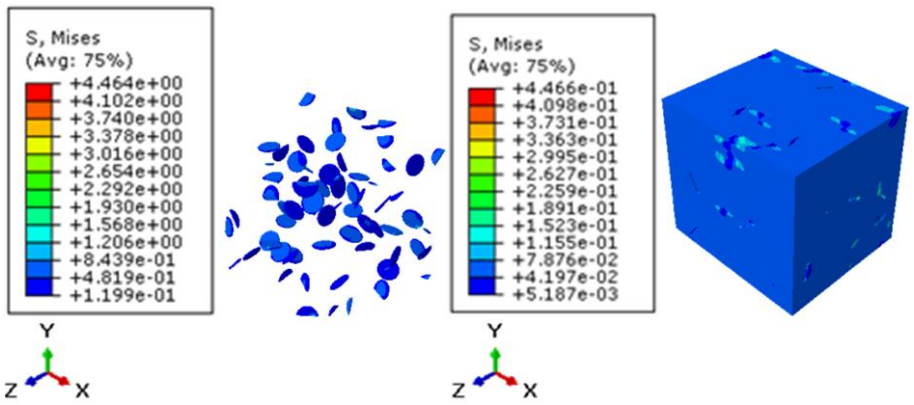

(a)

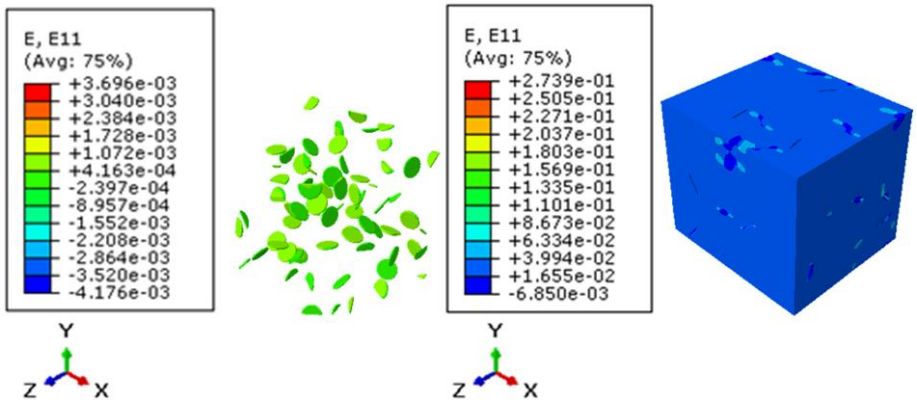

(b)

Figure 16 *Illustration of contour plots for AR=10^{-1} and* v_f *=0.01 :* (a) *Mises stress* (b) *uniaxial strain.*

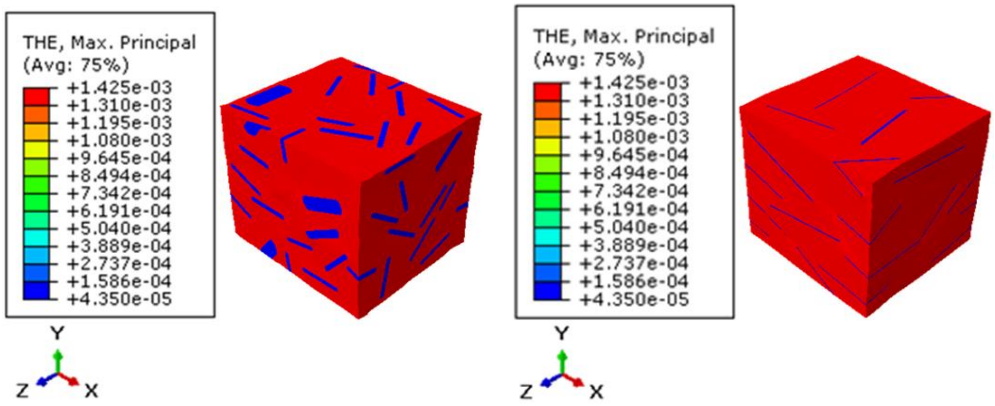

(a) (b)

Figure 17 *Illustration of thermal strain contour plots for* v_f *= 0.1:* (a) *AR=10^{-1}* (b) *AR=10^{-2}.*

5.2.2 *Aligned inclusions microstructure*

For the aligned microstructure (Figure 18), the anisotropy, in the FE Young's moduli and Poisson's ratio is presented. Comparison of the numerical versus the analytical OS and MS modelling are shown. Figure 19 depicts the contours plots of the Mises stress for traction loads in three directions. Results presented in Figure 20, indicate that OS and numerical model are in more agreement than the MS ones, which is excepted since FEA, as does OS, does not take into account interactions as regards to Eq.(12) between neighbouring inclusions.

(a) (b)

Figure 18 *Aligned GPL reinforced RVE for AR=10^{-1} and* v_f *=0.1:* (a) *graphene platelets and* (b) *numerical model.*

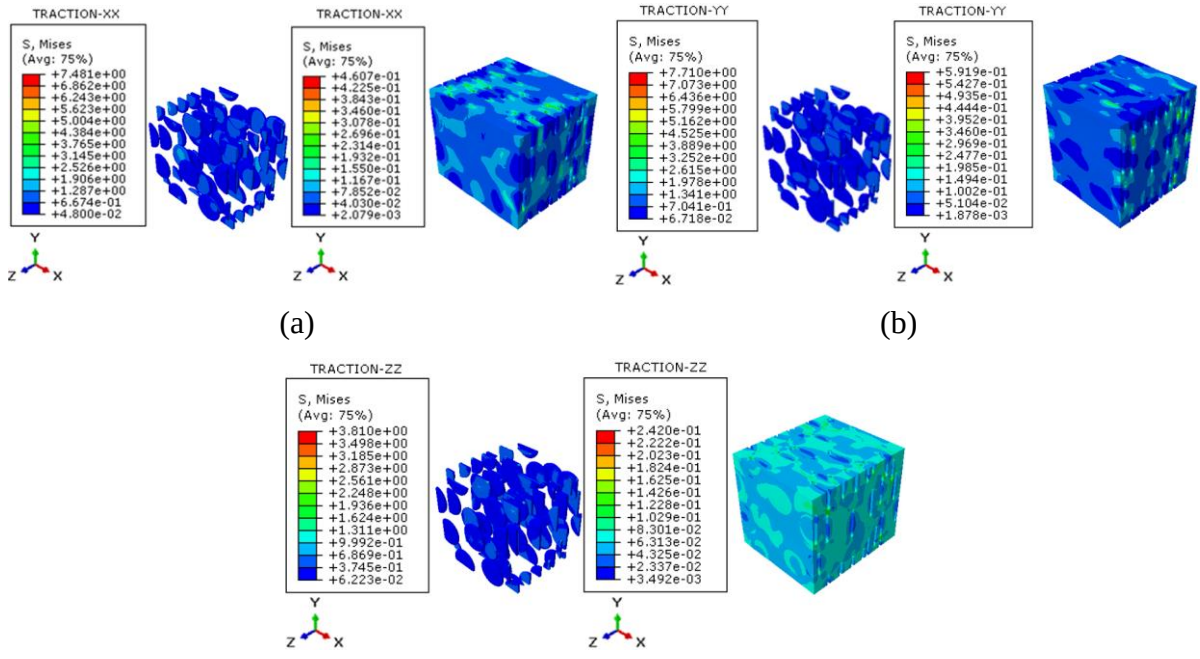

(a) (b)

(c)

Figure 19 *Illustration of Mises stress contour plots for AR=10^{-1} and* v_f *= 0.1:* (a) *x-x traction,* (b) *y-y traction, and* (b) *z-z- traction.*

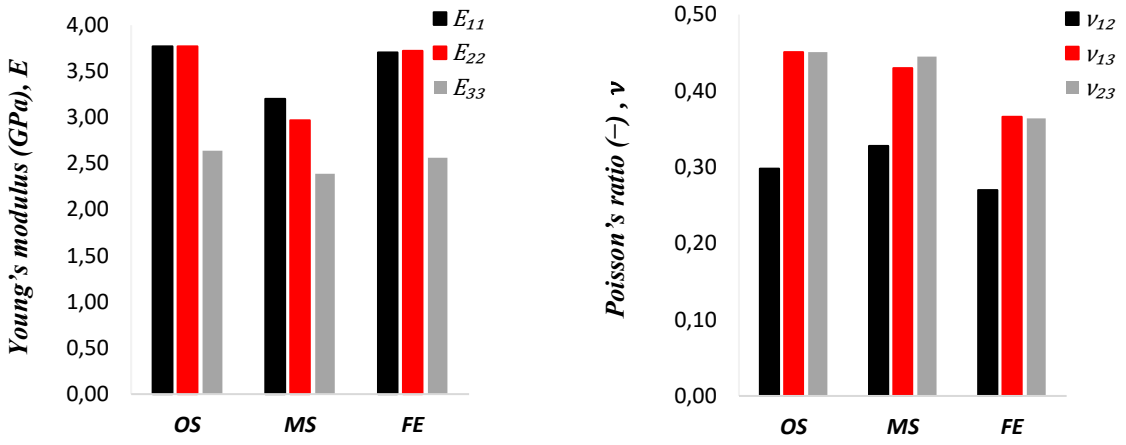

(a) (b)

Figure 20 *Comparison between analytical OS, MS and numerical results for aligned inclusions GPL/PA6 composite of AR=10^{-1} and* v_f *=0.1.*

6 Conclusion

A framework for investigating thermoelastic properties of graphene nanocomposites has been developed. The presented method is capable of estimating the properties for understanding and designing this type of materials. Interactions between embedded GPLs ignored by most of the available literature, are accounted for in the model using micromechanics-based Multi-site (MS) scheme for the case of aligned inclusions. Analytical One-site (OS) scheme is also utilised to derive properties of both spatial randomly-oriented and aligned microstructures. In addition to the analytical investigation, numerical characterisation using finite element modelling (FEM) is also performed.

Results carried out highlight the importance of the aspect ratio (AR) and volume fraction v_f, taking into account the inclusions' interaction with their neighbourhood in the MS modelling of ordered microstructures. For randomly-oriented inclusions, the comparison between analytical One-site (OS) and numerical results generally demonstrate fair agreement of the elastic modulus. On the other hand, the analytical results of the coefficient of thermal expansion (CTE) and Poisson's ratio tend to be higher than those of the numerical model. However, both analytical and numerical CTE results become in more agreement when AR =10^{-2}. Most effective reinforcement is observed with the low value of the aspect ratio.

The volume fraction also shows a significant influence on the overall behaviour, the higher the volume fraction, the higher the elastic stiffness. It should also be noted; except for when AR

$=10^{-2}$, higher volume fraction increases analytical CTE results while decreases numerical CTE results. For aligned microstructure, the aspect ratio of 10^{-1} was studied. Results indicate a higher closeness of agreement between FEA and OS than MS. The similarity in results between OS and FEA could be attributed to the fact that both of them do not account for interactions between neighbouring inclusions, unlike MS.

In summary, the current work introduces a multi-site (MS) formulation model for the development of graphene nanocomposite materials and compared with One-site (OS) and FEA models. An algorithm is developed to predict thermo-elastic properties of desired graphene nanocomposite materials accurately. The suggested algorithm paves the way for efficient design and predictions of multiphase graphene-based polymer composites behaviours at a very low computational time and cost. Our work would further promote the development of such advanced materials to replace the conventional composites in several applications, e.g. structural and automotive applications.

7 Data availability

The data required to reproduce these findings cannot be shared at this time as the data also forms part of an ongoing study.

8 Appendix A: Python script used for Abaqus post-processing

```
#==========================================================================
#============== FieldOutputs and get Subsets ==============================
#==========================================================================

    S = LastFrame.fieldOutputs['S']
    E = LastFrame.fieldOutputs['E']
    TEMP = LastFrame.fieldOutputs['TEMP']
    THE  = LastFrame.fieldOutputs['THE']
    IVOL = LastFrame.fieldOutputs['IVOL']

    E_MATRIX = E.getSubset(region = MATRIX)
    S_MATRIX = S.getSubset(region = MATRIX)
    TEMP_MATRIX = TEMP.getSubset(region = MATRIX)
    THE_MATRIX = THE.getSubset(region = MATRIX)
    IVOL_MATRIX = IVOL.getSubset(region = MATRIX)

    E_INCLUSIONS = E.getSubset(region = INCLUSIONS)
    S_INCLUSIONS = S.getSubset(region = INCLUSIONS)
    TEMP_INCLUSIONS = TEMP.getSubset(region = INCLUSIONS)
    THE_INCLUSIONS = THE.getSubset(region = INCLUSIONS)
    IVOL_INCLUSIONS = IVOL.getSubset(region = INCLUSIONS)

```

```
#================================================================================
#============== FieldOutputs computation over Gauss integration points =========
#================================================================================
    GAUSS_M = len(S_MATRIX.values)
    GAUSS_I = len(S_INCLUSIONS.values)

    for i in xrange(0,GAUSS_I):
        volume_i = IVOL_INCLUSIONS.values[i].data
        VOL_TOTAL += volume_i
        VOL_TOTAL_I += volume_i
        AVE_E_I = AVE_E_I + volume_i*E_INCLUSIONS.values[i].data
        AVE_S_I = AVE_S_I + volume_i*S_INCLUSIONS.values[i].data
        AVE_TEMP_I = AVE_TEMP_I + volume_i*TEMP_INCLUSIONS.values[i].data
        AVE_THE_I = AVE_THE_I + volume_i*THE_INCLUSIONS.values[i].data

    for i in xrange(GAUSS_M):
        volume_i = IVOL_MATRIX.values[i].data
        VOL_TOTAL += volume_i
        VOL_TOTAL_M += volume_i
        AVE_E_M = AVE_E_M + volume_i*E_MATRIX.values[i].data
        AVE_S_M = AVE_S_M + volume_i*S_MATRIX.values[i].data
        AVE_TEMP_M = AVE_TEMP_M + volume_i*TEMP_MATRIX.values[i].data
        AVE_THE_M = AVE_THE_M + volume_i*THE_MATRIX.values[i].data
```

```
#================================================================================
#============== Macroscopic stress tensor =======================================
#================================================================================

    S_MACRO[0,0] = AVE_S_M[0] + AVE_S_I[0]
    S_MACRO[1,1] = AVE_S_M[1] + AVE_S_I[1]
    S_MACRO[2,2] = AVE_S_M[2] + AVE_S_I[2]
    S_MACRO[0,1] = AVE_S_M[3] + AVE_S_I[3]
    S_MACRO[1,0] = S_MACRO[0,1]
    S_MACRO[0,2] = AVE_S_M[4] + AVE_S_I[4]
    S_MACRO[2,0] = S_MACRO[0,2]
    S_MACRO[1,2] = AVE_S_M[5] + AVE_S_I[5]
    S_MACRO[2,1] = S_MACRO[1,2]

#================================================================================
#============== Macroscopic strain tensor =======================================
#================================================================================
    E_MACRO[0,0] = AVE_E_M[0] + AVE_E_I[0]
    E_MACRO[1,1] = AVE_E_M[1] + AVE_E_I[1]
    E_MACRO[2,2] = AVE_E_M[2] + AVE_E_I[2]
    E_MACRO[0,1] = AVE_E_M[3] + AVE_E_I[3]
    E_MACRO[1,0] = E_MACRO[0,1]
    E_MACRO[0,2] = AVE_E_M[4] + AVE_E_I[4]
    E_MACRO[2,0] = E_MACRO[0,2]
    E_MACRO[1,2] = AVE_E_M[5] + AVE_E_I[5]
    E_MACRO[2,1] = E_MACRO[1,2]
```

```
#==========================================================================
#============== Macroscopic thermal strain tensor ==========================
#==========================================================================

    THE_MACRO[0,0] = AVE_THE_M[0] + AVE_THE_I[0]
    THE_MACRO[1,1] = AVE_THE_M[1] + AVE_THE_I[1]
    THE_MACRO[2,2] = AVE_THE_M[2] + AVE_THE_I[2]
    THE_MACRO[0,1] = AVE_THE_M[3] + AVE_THE_I[3]
    THE_MACRO[1,0] = THE_MACRO[0,1]
    THE_MACRO[0,2] = AVE_THE_M[4] + AVE_THE_I[4]
    THE_MACRO[2,0] = THE_MACRO[0,2]
    THE_MACRO[1,2] = AVE_THE_M[5] + AVE_THE_I[5]
    THE_MACRO[2,1] = THE_MACRO[1,2]

#==========================================================================
#============== Macroscopic temperature value ==============================
#==========================================================================
    TEMP_MACRO = AVE_TEMP_I + AVE_TEMP_M
```

```
#==========================================================================
#============== Engineering coefficients computation ======================
#==========================================================================

    if stepName == "TRACTION-XX":
       E11 =   S_MACRO[0,0]/E_MACRO[0,0]
       nu12 = -(E_MACRO[1,1]/E_MACRO[0,0])
       nu13 = -(E_MACRO[2,2]/E_MACRO[0,0])
       alpha11 = THE_MACRO[0,0]/TEMP_MACRO
       return E11, nu12, nu13, alpha11

    if stepName == "TRACTION-YY":
       E22 =   S_MACRO[1,1]/E_MACRO[1,1]
       nu21 = -(E_MACRO[0,0]/E_MACRO[1,1])
       nu23 = -(E_MACRO[2,2]/E_MACRO[1,1])
       alpha22 = THE_MACRO[1,1]/TEMP_MACRO
       return E22, nu21, nu23, alpha22

    if stepName == "TRACTION-ZZ":
       E33 =   S_MACRO[2,2]/E_MACRO[2,2]
       nu31 = -(E_MACRO[0,0]/E_MACRO[2,2])
       nu32 = -(E_MACRO[1,1]/E_MACRO[2,2])
       alpha33 = THE_MACRO[2,2]/TEMP_MACRO
       return E33, nu31, nu32, alpha33

    if stepName == "SHEAR-XY":
       G12 =   0.5*(S_MACRO[0,1]/(E_MACRO[0,1]+E_MACRO[1,0]))
       return G12
```

References

2020a. http://www.goodfellow.com/E/Polyamide-Nylon-6.html, http://www.goodfellow.com. Goodfellow.

2020b. https://omnexus.specialchem.com/selection-guide/polyamide-pa-nylon/properties-pa6-pa66, https://omnexus.specialchem.com. Omnexus.

Ahaouari, K., 1990. Contribution à la modélisation de la thermoélasticité et de l'acoustoélasticité des matériaux microhétérogènes.
Ahaouari, K., Corvasce, F., Lipinski, P., Berveiller, M., 1990. Détermination des propriétésthermomécaniques des composites à matrice métallique. Mémoires et Études Scientifiques Revue de Métallurgie 87, 73-84.
Ahmad, S.R., Xue, C., Young, R.J., 2017. The mechanisms of reinforcement of polypropylene by graphene nanoplatelets. Materials Science and Engineering: B, 2-9.
Azoti, W.L., Elmarakbi, A., 2017. Multiscale modelling of graphene platelets-based nanocomposite materials. Composite Structures 168, 313-321.
Azoti, W.L., Koutsawa, Y., Tchalla, A., Makradi, A., Belouettar, S., 2015. Micromechanics-based multi-site modeling of elastoplastic behavior of composite materials. International Journal of Solids and Structures 59, 198-207.
Boothroyd, S.C., Johnson, D.W., Weir, M.P., Reynolds, C.D., Hart, J.M., Smith, A.J., Clarke, N., Thompson, R.L., Coleman, K.S., 2018. Controlled Structure Evolution of Graphene Networks in Polymer Composites. Chemestry of Materials, 1524-1531.
Broohm, A., Zattarin, P., Lipinski, P., 2000. Prediction of mechanical behaviour of inhomogeneous and anisotropic materials using an incremental scheme. Archives of Mechanics 52, 949-967.
Cho, J., Luo, J.J., Daniel, I.M., 2007. Mechanical characterization of graphite/epoxy nanocomposites by multi-scale analysis. Composites Science and Technology 67, 2399-2407.
Dai, G., Jr., L.M., 2013. Damage evolution in nanoclay-reinforced polymers: A three-dimensional computational study. Composites Science and Technology 74, 67-77.
Dai, G., Jr., L.M., 2014. Graphene reinforced nanocomposites: 3D simulation of damage and fracture. Computational Materials Science 95, 684-692.
DassaultSystèmes, 2014. Abaqus 6.14 Scripting User's Guide.
Doghri, I., Ouaar, A., 2003. Homogenization of two-phase elasto-plastic composite materials and structures Study of tangent operators, cyclic plasticity and numerical algorithms. International Journal of Solids and Structures 40, 1681-1712.
Eshelby, J.D., 1957. The Determination of the Elastic Field of an Ellipsoidal Inclusion, and Related Problems, Proceedings Mathematical Physical & Engineering Sciences. The Royal Society, pp. 376-396.
Fassi-Fehri, O., A. Hihi, M.B., 1989. Multiple site self-consistent scheme. International Journal of Engineering and Science 27, 495-502.
Feng, C., Wang, Y., Kitipornchai, S., Yang, J., 2017. Effects of Reorientation of Graphene Platelets (GPLs) on Young's Modulus of Polymer Nanocomposites under Uni-Axial Stretching. polymers 9.
Feng, C., Wang, Y., Yang, J., 2018. Effects of Reorientation of Graphene Platelets (GPLs) on Young's Modulus of Polymer Composites under Bi-Axial Stretching. Nanomaterials 8.
Ferrari, M., 1991. Asymmetry and the high concentration limit of the Mori–Tanaka effective medium theory. Mechanics of Materials 11, 251-256.
Fisher, D.J., 2018. Negative Thermal Expansion Materials. Materials Research Forum LLC.
Gaitonde, V.N., Karnik, S.R., Mata, F., Davim, J.P., 2010. Modeling and Analysis of Machinability Characteristics in PA6 and PA66 GF30 Polyamides through Artificial Neural Network. Journal of Thermoplastic Composite Materials 23, 313-336.
Georgantzino, S.K., Giannopoulos, G.I., Anifantis, N.K., 2017. Thermoelastic Analysis of Graphene-Based Nanomaterials. Journal of Computations & Modelling.
Gong, G., 2018. Literature study of graphene modified polymeric composites.
Hill, R., 1963. Elastic properties of reinforced solids: some theoretical principles. Journal of the Mechanics and Physics of Solids, 357-372.

Jr., L.M., Dai, G., 2014. Hybrid and hierarchical nanoreinforced polymer composites: Computational modelling of structure–properties relationships. Composite Structures 117, 15-168.
Kpobie, W., Khlifa, S.B., Bonfoh, N., Fendler, M., Lipinski, P., 2012. Multi-site micromechanical modelling of thermo-elastic properties of heterogeneous materials. Composite Structures 94, 2068-2077.
Kroner, E., 1980. Graded and Perfect Disorder in Random Media Elasticity. Journal of the Engineering Mechanics 106, 889-914.
Kröner, E., 1973. Zur Klassichen Theorie Statistisch aufgebauter Festkörper. Internatinoal Jouranal of Engineering and Science 11, 171-191.
Kröner, E., 1977. Bounds for effective elastic moduli of disordered materials Journal of the Mechanics and Physics of Solids 25, 137-155.
Lee, C., Wei, X., Kysar, J.W., Hone, J., 2008. Measurement of the elastic properties and intrinsic strength of monolayer graphene. 321, 385-388.
Li, D., Liu, Y., Ma, H., Wang, Y., Wang, L., Xie, Z., 2015a. Preparation and properties of aligned graphene composites. Royal Society of Chemistry (RSC) Advances.
Li, Z., Young, R.J., Kinloch, I.A., Wilson, N.R., Marsden, A.J., Raju, A.P.A., 2015b. Quantitative determination of the spatial orientation of graphene by polarized Raman spectroscopy. Carbon 88, 215-224.
Li, Z., Young, R.J., Wilson, N.R., Kinloch, I.A., Valéls, C., Li, Z., 2016. Effect of the orientation of graphene-based nanoplatelets upon the Young's modulus of nanocomposites. Composites Science and Technology 123, 125-133.
Liu, H., Brinson, L.C., 2008. Reinforcing efficiency of nanoparticles: A simple comparison for polymer nanocomposites. Composites Science and Technology 68, 1502-1512.
Mandel, J., 1971. Plasticité classique et viscoplasticité. CISMCourses and Lectures
Mann, S., Kumara, R., Jindal, V.K., 2017. Negative thermal expansion of pure and doped graphene. RSC Advances.
MSC, 2016. Digimat User's Manual, E-xstream Engineering.
Papageorgiou, D.G., Kinloch, I.A., Young, R.J., 2016. Hybrid multifunctional graphene/glass-fibre polypropylene composites. Composites Science and Technology 137, 44-51.
Rouby, D., 2005. Coefficients de dilatation thermique et d'expansion hygrometrique et d'expansion hygrometrique. Micromecanique des composites μE1.
Sadowski, P., Kowalczyk-Gajewska, K., Stupkiewicz, S., 2015. Classical estimates of the effective thermoelastic properties of copper–graphene composites. Composites Part B: Engineering 80, 278-290.
Shi, Z., Li, X.-F., Bai, H., Xu, W.-W., Yang, S.-Y., Lu, Y., Han, J.-J., Wang, C.-P., Liu, X.-J., Li, W.-B., 2016. Influence of microstructural features on thermal expansion coefficient in graphene/epoxy composites. Heliyon 2.
Shiu, S.-C., Tsai, J.-L., 2014. Characterizing thermal and mechanical properties of graphene/epoxy nanocomposites. Composites Part B: Engineering 56, 691-697.
Shokrieh, M.M., Esmkhani, M., Shokrieh, Z., Zhao, Z., 2014. Stiffness prediction of graphene nanoplatelet/epoxy nanocomposites by a combined molecular dynamics–micromechanics method. Computational Materials Science 92, 444-450.
Su, Y., Li, J.J., Weng, G.J., 2018. Theory of thermal conductivity of graphene-polymer nanocomposites with interfacial Kapitza resistance and graphene-graphene contact resistance. Carbon, 137, 222-233.
Torquato, S., 1997. Effective stiffness tensor of composite media-I. Exact series expansions. Journal of the Mechanics and Physics of Solids 45, 1421-1448.
Torquato, S., 2002. Random Heterogeneous Materials: Microstructure and Macroscopic Properties. New York: Springer-Verlag.

Wang, T.-Y., Tseng, P.-Y., Tsai, J.-L., 2018. Characterization of Young's modulus and thermal conductivity of graphene/epoxy nanocomposites. Journal of Composite Materials 53, 835-847.
Wejrzanowski, T., Grybczuk, M., Chmielewski, M., Pietrzak, K., Kurzydlowski, K.J., Strojny-Nedza, A., 2016. Thermal conductivity of metal-graphene composites. Materials and Design, 163-173.
Weon, J.-I., Sue, H.-J., 2005. Effects of clay orientation and aspect ratio on mechanical behavior of nylon-6 nanocomposite. Polymer 46.
Xiao, W., Zhai, X., Ma, P., Fan, T., Li, X., 2018. Numerical study on the thermal behavior of graphene nanoplatelets/epoxy composites. Results in Physics 9, 673-679.
Yoon, D., Son, Y.-W., Cheong, H., 2011. Negative Thermal Expansion Coefficient of Graphene Measured by Raman Spectroscopy. Nano Letters 11, 3227-3231.
Young, R.J., Liu, M., Kinloch, I.A., Li, S., Zhao, X., Vallés, C., Papageorgiou, D.G., 2018. The mechanics of reinforcement of polymers by graphene nanoplatelets. Composites Science and Technology 154, 110-116.
Zarasvand, K.A., Golestanian, H., 2017. Investigating the effects of number and distribution of GNP layers on graphene reinforced polymer properties: Physical, numerical and micromechanical methods. Composites Science and Technology, 117-126.
Zattarin, P., 2000. Étude de l'intégration d'un modèle polycristallin dans un code d'éléments finis en élastoplasticité.
Zhang, Y.-F., Zhao, Y.-H., Bai, S.-L., Yuan, X., 2016. Numerical simulation of thermal conductivity of graphene filled polymer composites. Composites Part B 106, 324-331.

Author contributions

A. Elmasry and W. Azoti developed the workflow and original script preparations, methodology, coding and programming, discussions and significance of the results. W. Azoti conceived the project conceptualization. W. Azoti and M. Elmarakbi performed Software numerical simulations and detailed analysis. A. Elmasry performed validation of models and documentation. A. Elmarakbi supervised and managed the overall work. A. Elmarakbi prepared methodology and working approach, and conducted detailed discussions and significance of the results. All the authors contributed to the writing and revising of the manuscript.

Additional information

Correspondence and requests for materials should be addressed to A. Elmasry (ahmed.elmasry@northumbria.ac.uk).